DEVELOPMENT OF NEW CHEMICAL PROCESSES TO LEAD-FREE PIEZOELECTRIC AND FERROELECTRIC MATERIALS

by

Amanda Gronotte
B. Sc., Simon Fraser University, 2006

THESIS SUBMITTED IN PARTIAL FULFILLMENT OF
THE REQUIREMENTS FOR THE DEGREE OF

MASTER OF SCIENCE

In the Department
of
Chemistry

SIMON FRASER UNIVERSITY

Fall 2009

APPROVAL

Name: **Amanda Gronotte**

Degree: **Master of Science**

Title of Thesis: **Development of New Chemical Processes to Lead-Free Piezoelectric and Ferroelectric Materials.**

Examining Committee:

Chair: **Zuo-Guang Ye**
[Correct title – Consult your Grad Secretary/Assistant

_____

Zuo-Guang Ye
Senior Supervisor
Correct title – Consult your Grad Secretary/Assistant

_____

Steven Holdcroft
Supervisor
Correct title – Consult your Grad Secretary/Assistant

_____

Hogan Yu
Supervisor
Correct title – Consult your Grad Secretary/Assistant

_____

Tim Storr
Internal Examiner
Correct title – Consult your Grad Secretary/Assistant
University or Company (if other than SFU)

Date Defended/Approved: November-27-2009

Declaration of
Partial Copyright Licence

ABSTRACT

In our efforts to develop new lead-free piezoelectric materials, $K_{0.5}Na_{0.5}NbO_3$ (KNN)-based ceramics were prepared by a new solid-state synthetic method using potassium fluoride (KF) as a sintering agent. The addition of KF resulted in ceramics with enhanced density and quality. Piezoelectric properties were improved over those of conventionally sintered KNN ceramics. Chemical analyses were performed by means of Energy Dispersive Spectroscopy (EDS) and X-ray Photoelectron Spectroscopy (XPS) to deduce the sintering mechanism.

The ferroelectric solid-solution of $(1-x)(K_{0.5}Na_{0.5})NbO_3$-$x$$BiAlO_3$ was synthesized by solid state reaction. A partial temperature-composition phase diagram was established, which includes a morphotropic phase boundary in the composition range $0.002 \leq x \leq 0.005$. Due to increased chemical and polar disorders, which are a result of the coupled substitutions: $Bi^{3+} + Al^{3+} \rightarrow (K_{0.5}Na_{0.5})^{+} + Nb^{5+}$, the temperature dependences of dielectric constant exhibit increasingly broadened peaks and significant frequency dispersion as the BA concentration increases.

This thesis is dedicated to

my beloved grandfather, Robert Henry Gronotte,

whose love of science has been apparent

for as long as I can remember.

ACKNOWLEDGEMENTS

It is an honor for me to thank my senior supervisor, Dr. Zuo-Guang Ye. His encouragement, guidance and support from the initial to final stages of my graduate studies, enabled me to develop an understanding of the subject along with skills that will benefit me throughout the course of my life.

I would like to thank my supervisory committee members, Dr. Steven Holdcroft and Dr. Hogan Yu, for their valuable questions and advice during the course of this work.

I extend my thanks to Dr. Tim Storr for agreeing to be the internal examiner of my thesis.

I am grateful to Bryan Wood for assistance with SEM, Michael Wang for assistance with XPS, and Nathanael Sieb for assistance with EDS.

I would like to express my gratitude to the members of Dr. Ye's research group, both past and present. In particular, it is my pleasure to thank Mr. Hamel Tailor for his helpful discussion, support and friendship. I am also grateful to Dr. Chao Lei, Dr. Weimin Zhu, Dr. Haiyan Guo, Dr. Alexei Bokov, Mr. Allen Wei, and the late Mr. Huichun Yu.

I would like to thank the members of the Chemistry Department at Simon Fraser University for their support.

The financial supports from Simon Fraser University, the Chemistry Department, the Natural Sciences and Engineering Research Council of Canada, and the U. S. Office of Naval Research are greatly appreciated.

Finally, I owe my deepest gratitude to my loving family and friends. Dad and Judi, Mom and Rob, your patience, understanding, motivation, guidance, support and most importantly, love has made this accomplishment possible. Bobby, you are my brother and dearest friend. Thank you for always being there for me. Josh, Janelle and David, you may be ‘the little kids”, but you play a very “large” role in my life. Aunt Marianne and Uncle Paul, thank you for always inspiring me to strive for more. Eleni, Sheri, Susan, Nicholas, Arseniy, and Armstrong, thank you for your friendship. I love you all.

TABLE OF CONTENTS

LIST OF FIGURES

LIST OF TABLES

LIST OF ABBREVIATIONS

BA	$BiAlO_3$
BT	$BaTiO_3$
d_{33}	piezoelectric coefficient
E_C	coercive field
E'_C	apparent coercive field
EDS	energy dispersive spectroscopy
ε'	real part of permittivity
ε''	imaginary part of permittivity
ε'_{max}	maximum dielectric constant
ε'_{RT}	room temperature dielectric constant
f_a	antiresonance frequency
f_r	resonance frequency
KNN	$(K_{0.5}Na_{0.5})NbO_3$
k_P	electromechanical coupling factor
LFD	low frequency dispersion
MPB	morphotropic phase boundary
NBT	$(Na_{0.5}Bi_{0.5})TiO_3$
PLZT	$(Pb,La)(Zr,Ti)O_3$
P_i	local polarization
P_s	spontaneous polarization
P_r	remnant polarization
P'_r	apparent remnant polarization
PMN-PT	$Pb(Mg_{1/3}Nb_{2/3})O_3$-$PbTiO_3$
PT	$PbTiO_3$
PZT	$Pb(Zr,Ti)O_3$

SEM	scanning electron microscopy
$tan\delta$	dielectric loss
T_1	polymorphic phase transition temperature
T_C	Curie temperature
T_{max}	maximum permittivity temperature
$T_{T\text{-}O}$	tetragonal to orthorhombic phase transition temperature
XPS	x-ray photoelectron spectroscopy
XRD	x-ray diffraction

CHAPTER 1:
General Introduction

This thesis work contains various ways of synthesizing, developing, and improving lead-free piezoelectric ceramics with high performance and high Curie temperatures for a wide range of applications as electromechanical transducers, sensors and actuators.

This chapter will present the basic concepts and background information which lay out the foundation of our work. It includes ferroelectricity, piezoelectricity, the perovskite structure, ceramic sintering, and a few examples of the most promising lead-free ferroelectric materials, leading to the motivation and objectives of our work.

1.1 Ferroelectricity

A ferroelectric material is one that exhibits a spontaneous electric polarization (P_s), over some range of temperature, that can be reoriented with the application of an appropriate external electric field [1]. Ferroelectric materials are characterized by a hysteresis loop (Fig. 1.1), which displays the variation of polarization (P) as a function of applied electric field (E) [2].

As shown in Figure 1.1, when a relatively small electric field is first applied to a ferroelectric material, it behaves as a normal dielectric and displays a linear response between polarization and electric field. However, as the field increases, domains (regions of neighboring unit cells with the same polarization direction) not originally aligned with the field begin to reorient in the direction of the applied field, which results in a rapid increase in polarization until all are aligned and the polarization is saturated. When the

external electric field is reversed, some polarization will return to the original state, however, a large component will remain in the direction of the previously applied field, exhibiting a remnant polarization (P_r) at zero electric field. As the field is reversed, the polarization can be completely reversed to $-P_r$. It is this field that is termed the coercive field (E_c). The polarization can be saturated once again in the opposite direction upon increasing the reversed field strength further. The loop can be completed by then switching the direction of the applied field and increasing to the saturation point of the polarization.

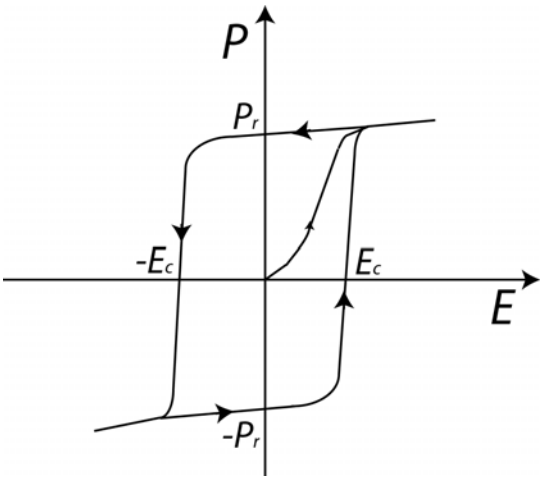

Figure 1.1: A typical Polarization-Electric Field (*P-E*) hysteresis loop produced by ferroelectric materials.

The electric polarization obtained from ferroelectric materials may be the result of three contributions: (1) a dielectric contribution, (2) a polarization (domain) switching contribution, and/or (3) a leakage current contribution. Figure 1.2 shows the respective *P-E* hysteresis loops that are produced as a result of each contribution. The dielectric contribution produces a polarization that is directly proportional to the external electric field, resulting in a linear relationship (Fig. 1.2(a)), the polarization switching

contribution exhibits a rectangular loop (Fig. 1.2(b)), and the leakage contribution displays an ellipse shape (Fig. 1.2(c)). Because each of these contributions exhibits different *P-E* hysteresis loops, the shape of the loop for different materials will vary with the amount and type of contributions present.

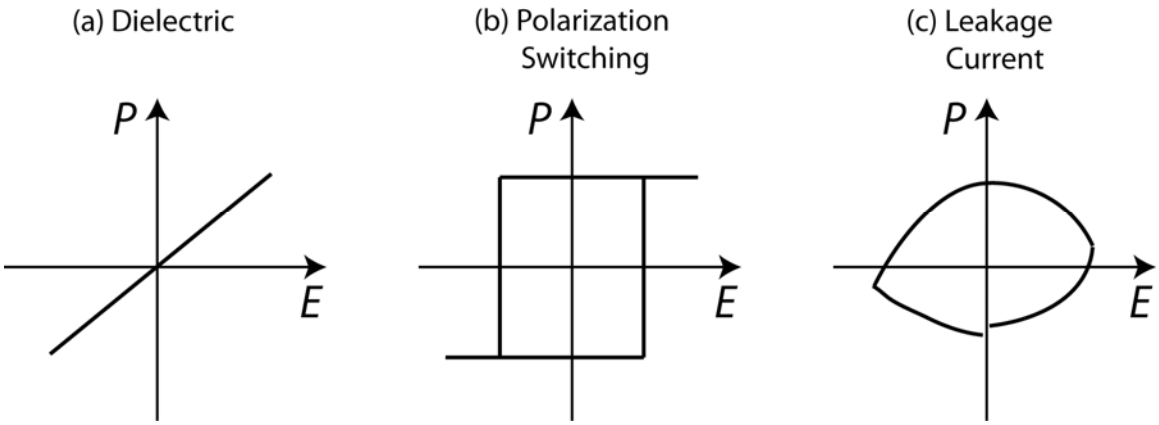

Figure 1.2: Components of a ferroelectric hysteresis loop: (a) Dielectric, (b) Polarization Switching and (c) Leakage current (schematic).

The spontaneous polarization of ferroelectric materials is exhibited over a certain temperature range specific to each material. Within this temperature range the material can undergo various structural phase transitions. The temperature at which the material changes from a ferroelectric, polar and non-centrosymmetric phase to a paraelectric, non-polar and centrosymmetric phase, is called the Curie temperature (T_C). Because the material is centrosymmetric and non-polar above the T_C, there are no possible polarization states (Fig. 1.3(c)), therefore, the material is unable to exhibit a spontaneous polarization or the ferroelectric effect. Below T_C, the structure becomes distorted, breaking the symmetry of the paraelectric structure, allowing for multiple polarization states and permitting the existence of ferroelectricity in the material (see Sec. 1.4 for the

structural origin of ferroelectricity). This is shown in Figure 1.3(a) by the two minima separated by a potential energy barrier (ΔE) [3].

The temperature dependences of dielectric, elastic, thermal, and optical properties often show anomalies around phase transition temperatures due to low potential energy barriers (Fig. 1.3(b)) [2]. A good example is the large increase in dielectric permittivity (ε') observed at T_C (Fig. 1.3(d)), resulting from an extremely polarizable state due to structural instability. This sharp increase in permittivity is indicative of a ferroelectric to paraelectric phase transition.

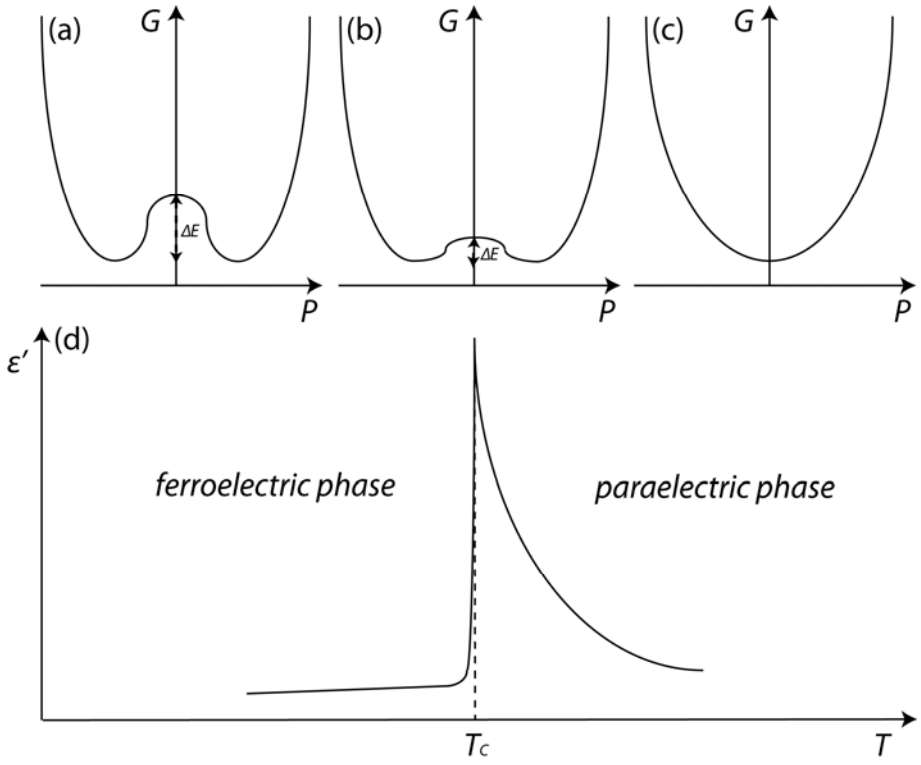

Figure 1.3: Top: Free energy (*G*) as a function of polarization (*P*) at various temperatures (*T*): (a) $T<T_C$, (b) $T=T_C$, and (c) $T>T_C$ (adapted from Ref. [3]).
Bottom: (d) Typical variation of dielectric permittivity (ε') as a function of temperature for a normal ferroelectric.

1.2 Piezoelectricity

In 1880, the Curie brothers found that certain materials had the ability to generate an electric potential in response to an applied mechanical stress [4]. This "direct" effect was also found to be reversible because these materials also changed shape under the application of an external electric field and, therefore, exhibited a "converse" effect. Any material that is polarizable is able to exhibit both the direct and converse effects, which together are known as the piezoelectric effect. Figure 1.4 shows the molecular mechanism of the piezoelectric effect with respect to the ions in a perovskite crystal structure of $BaTiO_3$.

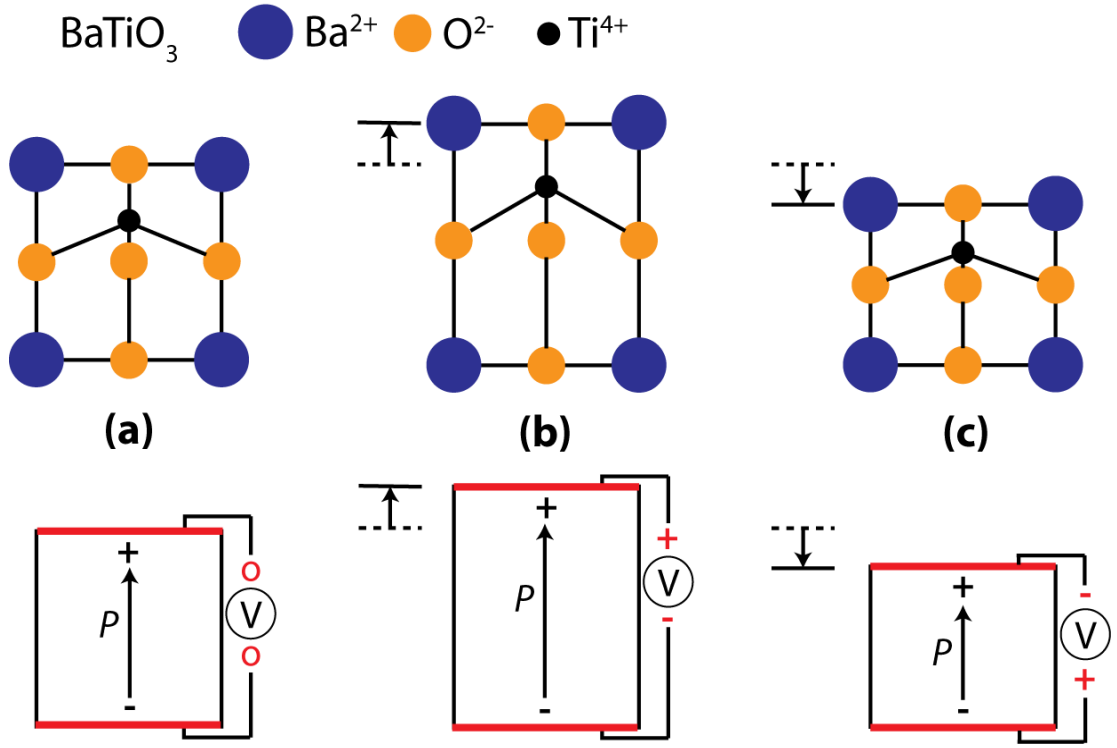

Figure 1.4: The mechanism of the piezoelectric effect. Top: 2-dimensional perovskite structure of $BaTiO_3$ in response to an external electric field. Bottom: Magnitude of polarization (*P*) with response to an external electric field. (a) room temperature structure and *P* under no external field, (b) elongated structure and increased *P* under external field of same polarity as *P*, and (c) compressed structure and decreased *P* under external field of opposite polarity as *P*.

The direct and converse piezoelectric effects can be described by the following equations [5]:

$$D_i = d_{ijk} X_{jk} \quad \text{(Direct effect)} \quad , \tag{1.1}$$

$$x_{ij} = d_{kij} E_k \quad \text{(Converse effect)} \quad , \tag{1.2}$$

where X_{ij} is the stress applied to a piezoelectric material, and D_i is the induced charge density, E_k is the electric field applied, and x_{ij} is the strain developed in the piezoelectric material, and d_{ijk} and d_{kij} are piezoelectric coefficients with units of C/N and m/V, respectively. Both d_{ijk} and d_{kij} are third-rank tensors, however, these piezoelectric coefficients for the direct and converse effects are thermodynamically identical.

Equations 1 and 2 can be simplified and may be expressed in the reduced notation form [6]:

$$D_i = d_{im} X_m \quad , \tag{1.3}$$

$$x_m = d_{mi} E_i \quad , \tag{1.4}$$

where values of i=1, 2, or 3 and values of m=1, 2, 3, 4, 5, or 6, which are directional values, because all of the properties in the above equations are directional properties [7]. The values of i and m identify the geometries under which the properties are measured (Fig. 1.5(a)). For example, d_{31} is measured when the induced polarization is generated in direction 3 due to a stress applied in direction 1, or when the induced strain is in direction 3 due to an electric field applied in direction 1. For a thin ceramic disc, d_{33} is measured because the output signal is produced in the same direction as the stress is applied (Fig. 1.5(b)). It is important to note that the strain and stress tensors are symmetrical, therefore, the piezoelectric coefficient is also symmetrical with respect to the same i and m values

($d_{im} = d_{mi}$). High piezoelectric coefficients are desirable in order to increase the charge or strain developed per force or electric field applied.

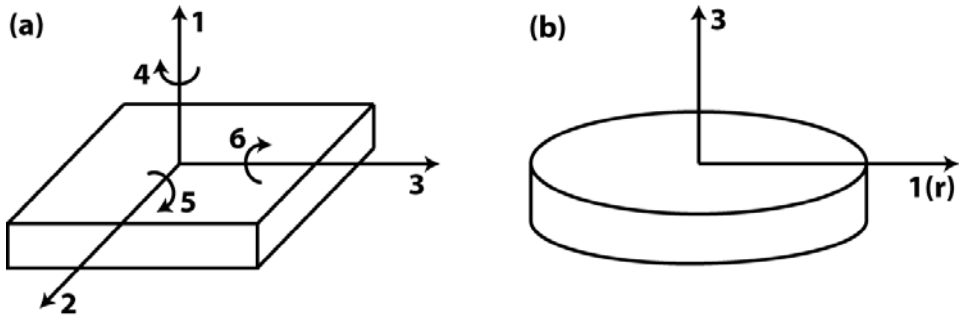

Figure 1.5: (a) Directional axes for a plate, and (b) directional axes for a thin disc, where 1(r) is the radial direction.

Another important parameter used to characterize piezoelectric performance is the electromechanical coupling factor (k). This term is a measure of the ability of a piezoelectric material to convert mechanical energy to electrical energy or vice versa:

$$k = \sqrt{(\text{generated mechanical energy/supplied electrical energy})} \quad (1.5)$$

$$k = \sqrt{(\text{generated electrical energy/supplied mechanical energy})} \quad (1.6)$$

A unity value of k would represent perfect energy conversion, so a value close to this is desired. Like the piezoelectric coefficient, the electromechanical coupling factor is also a directional property, so subscripts are used to indicate the geometry under which the property is determined, e.g. k_{33} or k_{31}. For certain shapes, special indices are used. For example, for a thin ceramic disc, the planar coupling factor (k_p) is a measure of radial coupling between an electric field applied in direction 3 and the mechanical vibrations produced radially in directions **1(*r*)** (see Fig. 1.5(b)) [8].

1.3 Applications of Piezo- and Ferroelectric Materials

The ability of materials to show good piezoelectric properties has led to many industrial and commercial applications, such as actuators, sensors and transducers. The ability of these materials to generate strain makes them useful as high precision actuators, which are used in the fabrications of sonar and ultrasound imaging, diagnosis and treatment. Piezoelectric actuators find applications in scientific instrumental techniques like Atomic Force Microscopy (AFM). These materials are widely utilized as sensors because they have the ability to generate an electric signal in response to stress, acoustic waves, or vibrations. Applications in sonar and ultrasound detection are very typical of these types of materials. Piezoelectrics are also very common in our daily life. For example, they are used in gas igniters, ink jet printers, frequency standards, such as quartz clocks, and in many automotive applications, such as airbag deployment.

Ferroelectric materials are widely used as capacitors due to their very high dielectric permittivity values, which are commonly exhibited. They are also used in memory applications, such as non-volatile ferroelectric RAM as a result of their hysteretic properties (switchable spontaneous polarization). The spontaneous polarization of ferroelectrics also changes with temperature, which makes them pyroelectrics. These materials generate electric potential (or current) with temperature change, making them useful for heat sensing applications, such as infrared (IR) detection.

1.4 Perovskite Structure

Today, a vast majority of ferroelectric materials in applications are of the perovskite structure. Figure 1.6(a) shows a typical ABO_3 perovskite unit cell, which consists of the A cations at the corners of the cell and the B cation in the centre of an oxygen octahedron.

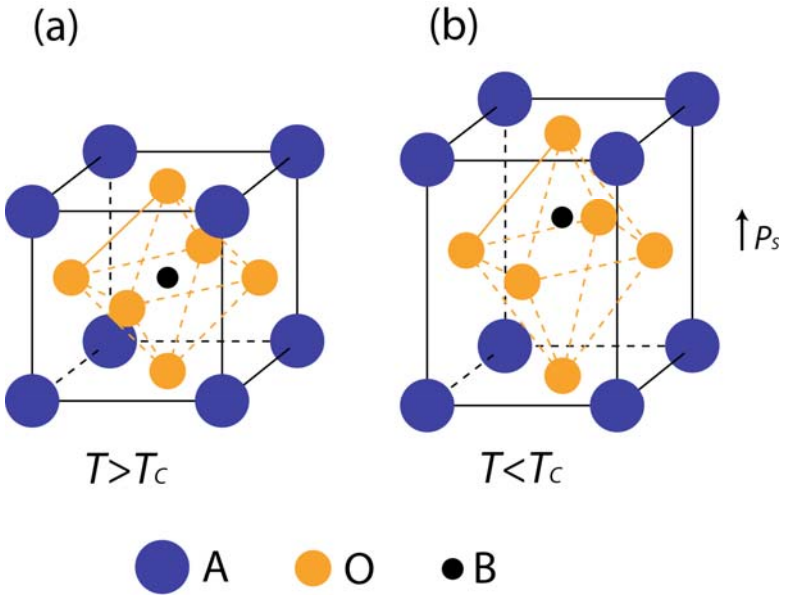

Figure 1.6: (a) Cubic prototype perovskite ABO_3 crystal structure above T_C; (b) distorted perovskite crystal structure below the T_C depicting the spontaneous polarization.

The stability of the ferroelectric phase will depend on bond type and polarizability, however, the stability of the structure is most sensitive to the size and valence of the A and B cations and is generally described with respect to ionic radii. The tolerance factor (t) is used to predict the formation of a stable perovskite structure [9].

$$t = \frac{r_A + r_O}{\sqrt{2}(r_B + r_O)} \quad , \tag{1.7}$$

where r_A, r_B, and r_O are the ionic radii of the A, B, and oxygen ions, respectively. It has been determined that the stability of the perovskite structure falls between t =0.88 and t =1.09 with the A cation having a coordination number of 12, and B cation a coordination number of 6 [2, 10].

When a perovskite ferroelectric material is heated above its Curie temperature, its structure is cubic and centrosymmetric, as discussed previously. However, when this material is below its Curie temperature, the structure becomes distorted, causing the B cations to be displaced with respect to the oxygen ions, which results in a spontaneous polarization (P_s) (Fig. 1.5(b)). The direction of this spontaneous polarization can be reoriented with the application of an external electric field of opposite polarity, which is characteristic of ferroelectric materials. In order to create a large polarization, B cations are typically small, highly charged ions like Ti^{4+}, Zr^{4+}, Sn^{4+}, Nb^{5+}, or Ta^{5+}, while A cations are generally large ions with low charge such as K^{+}, Ba^{2+}, Pb^{2+}, Bi^{3+}, or La^{3+}. The large A cations will facilitate the distortion for the small B cations to move off center and, therefore, create a large electric displacement and polarization.

1.5 Sintering of Ceramics

Sintering is a heat treatment process for making useful polycrystalline ceramics from a powder or porous material. Depending on the type of systems, there are several types of sintering methods. The first type is for pure, single phase, ceramic materials. The powder is pressed into a compact, which is then heated to a temperature approximately 50-80% of the melting temperature [11]. In this way, the powder does not melt; rather the particles join to reduce the porosity of the compact by ionic diffusion (Fig. 1.7).

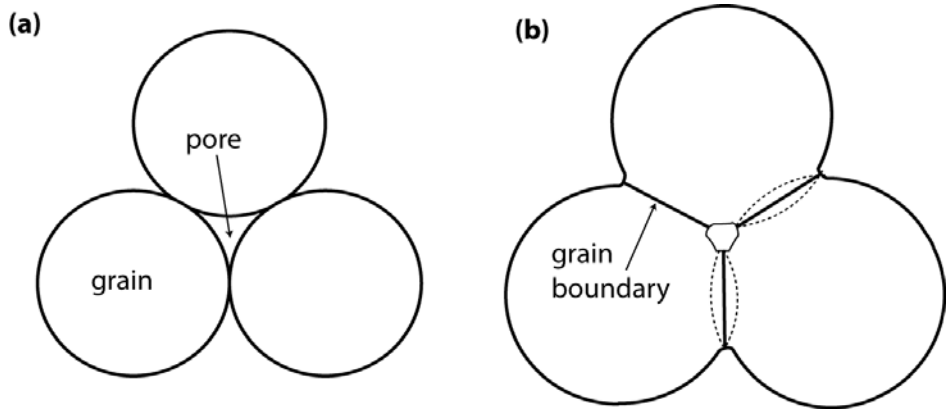

Figure 1.7: Schematics of sintering process: (a) three grains before solid-state sintering, and (b) after sintering.

Because this process occurs in the solid-state, this method is referred to as 'solid-state sintering'. This type of sintering, however, may not produce a dense ceramic in all cases, or the sintering temperature may be too high for practical reasons. Instead, an additive can be used, which forms a small amount of liquid phase between the particles at the sintering temperature. The liquid phase does not cause the density of the material to increase by filling the pores itself; it simply provides a high mobility path for atomic diffusion (Fig. 1.8) [11]. This method is appropriately termed 'liquid-phase sintering'.

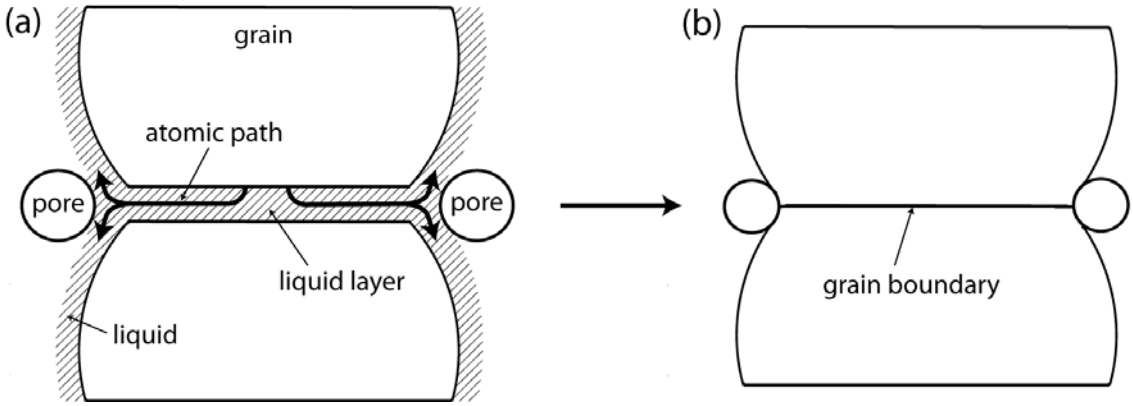

Figure 1.8: The liquid-phase sintering process.

Yet another common type of sintering is 'pressure-assisted sintering', which can be applied to either solid-state or liquid-phase sintering. This technique involves the application of an external pressure on the powder compact during heating.

It is very important to synthesize a dense ceramic as close to pore-free as possible in order to obtain high dielectric, piezoelectric and ferroelectric properties. Since air has a dielectric constant of 1 and a d_{33} of 0 pC/N at room temperature, these low values will cause the potential properties of ceramics to diminish. Therefore, the sintering process is a very important step in the fabrication of high-performance piezo-/ferroelectric ceramics. One of the main tasks of this thesis work is to develop new methods for the sintering of a class of important piezo- and ferroelectric materials.

1.6 Lead-Free Perovskite Ferroelectrics

Currently, lead containing ferroelectric solid solutions, such as $Pb(Zr,Ti)O_3$ (PZT) and $(Pb,La)(Zr,Ti)O_3$ (PLZT) have been shown to exhibit the best piezoelectric and ferroelectric properties, and as a result they are used widely in various technological, industrial and commercial applications [7]. These enhanced properties can be attributed to the $6s^2$ lone pair of electrons on the Pb^{2+} ion [12, 13]. For both $PbTiO_3$ (PT) and $BaTiO_3$ (BT), the ground state below the Curie temperature is a distorted tetragonal structure, which is due to their tolerance factors (1.019 and 1.062, respectively) being greater than 1, causing oxygen octahedral distortion and thus polarization. This distortion makes the molecular orbitals lose degeneracy and increase in energy, which causes the 6s orbital to mix with the 6p orbitals. Now the Pb^{2+} $6s^2$ electron pair resides in an s-p hybrid

orbital and are isolated to one side of the Pb^{2+} ion (Fig. 1.9) [12, 14], introducing inherent polarization.

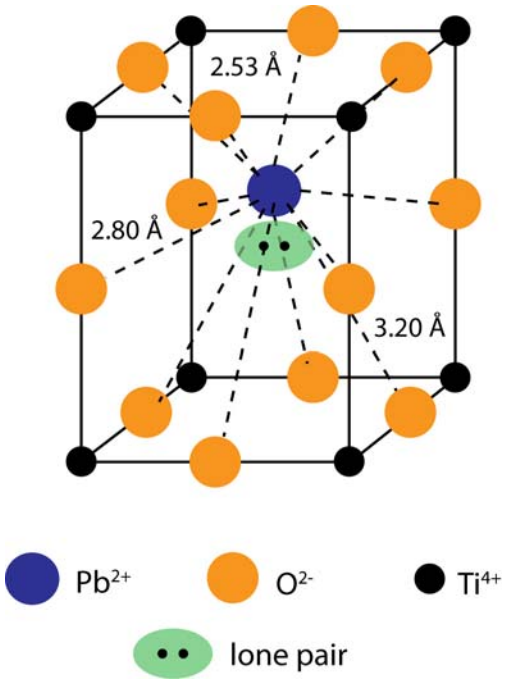

Figure 1.9: Perovskite structure showing the presence of the stereochemically active electron pair effect by the variation of Pb-O bond distances.

This stereochemically active lone pair promotes larger displacement than in $BaTiO_3$, for example, and results in a highly polarizable material. Confirmation of this effect can be obtained from the reported tetragonality (c/a ratio of the unit cell parameters) and T_C values of BT and PT, which are 1.01 and 120 ˚C [15], and 1.06 and ~490 ˚C [16], respectively. PT has a larger c/a ratio, indicating a larger structural distortion than BT, and it also has a much higher T_C than BT because much more thermal energy is required to stabilize a cubic perovskite structure for the more distorted PT. In this non-polar centrosymmetric structure, there is no distortion and the $6s^2$ electrons of Pb^{2+} reside in the spherical s-orbital and are stereochemically inactive.

The excellent properties of PZT and PLZT are also a result of the formation of a morphotropic phase boundary (MPB) between the rhombohedral and tetragonal phases of these materials, which are formed from solid solutions [7, 17]. An MPB is a region bridging two phases of different symmetry, in which these two separate phases and lower symmetry phases can coexist [17]. Electrical properties are often enhanced within an MPB due to the increased number of possible polarization directions as a result of the coupling of phases. Within this region, there is a greater chance for the dipole moments to align with an external electric field, which allows for optimum polarization reorientation, leading to a larger overall net polarization and, thereby, higher piezoelectric response in the material [18].

Unfortunately, these materials contain lead, which is toxic both environmentally and biologically. Legislation has been passed in Europe that restricts the use of six hazardous substances including lead. The Waste from Electrical and Electronic Equipment (WEEE) and the Restriction of Hazardous Substances (RoHS) directives became law in 2003 [19], which has encouraged the scientific community to develop lead-free alternatives. Unfortunately, the application of lead-free systems is limited due to the comparably low piezoelectric and ferroelectric performance and low depoling temperature, above which the material loses polarization and piezoelectricity. Some of the lead-free perovskite compounds currently being studied are $BaTiO_3$, $KNbO_3$, $(K_{0.5}Na_{0.5})NbO_3$, $(Na_{0.5}Bi_{0.5})TiO_3$ and other Bi-based systems.

1.6.1 $(K_{0.5}Na_{0.5})NbO_3$-Based Systems

This thesis work focuses on developing piezo-/ferroelectric materials that are lead-free. To replace lead-containing materials, alkali transition metal compounds, such as potassium niobate, $KNbO_3$, are an appropriate choice. Nb^{5+} is a small B-site cation (ionic radius of 0.64 Å [20]) with no d-electrons, which allows for stronger ionic bonding and a larger displacement. K^+ is a large A-site cation (ionic radius of 1.64 Å [20]), which causes the perovskite unit cell to expand, thereby allowing more space for Nb^{5+} to rattle in the TiO_6 octahedral, leading to a larger polarization. By forming a solid-solution with an MPB, this polarization can be further enhanced, as in PZT. As a matter of fact, the most promising of the lead-free materials is an alkali-transition metal solid-solution, potassium sodium niobate $(1-x)KNbO_3$-$xNaNbO_3$ (KNN).

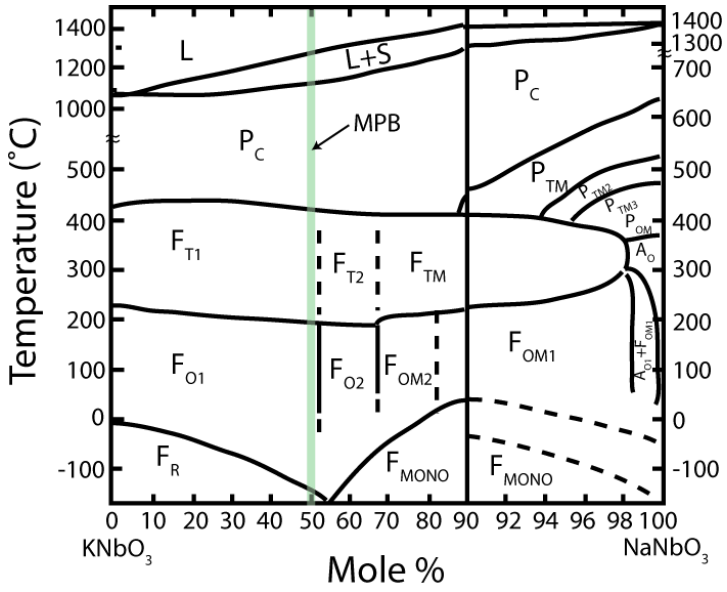

Figure 1.10: Temperature versus composition phase diagram of the $(1-x)KNbO_3$-$xNaNbO_3$ solid solution system (note the different scales for $x \leq 90\%$ and $x \geq 90\%$) (adapted from Ref. [23]).

KNN possess an MPB at x~0.5, which separates two different orthorhombic phases (F_{O1} and F_{O2}) at room temperature (Fig. 1.10) [21, 22]. It is at this composition that the optimum piezoelectric properties are exhibited [21, 22].

In fact, hot-pressed KNN ceramics have been reported to produce good piezoelectric properties with d_{33} and k_p values of 160 pC/N and 45%, respectively, along with a high Curie temperature of approximately 420 °C [21, 22, 24]. However, it is difficult to obtain dense ceramics of KNN by conventional sintering methods due to its high hygroscopicity and the volatility of K_2O at high temperatures, which usually drifts the composition away from stoichiometric [22, 24, 25].

Many research groups around the world have recently been investigating various KNN-based systems, including KNN-$LiNbO_3$ [26], KNN-$LiTaO_3$ [27], KNN-$LiSbO_3$ [28], KNN-$SrTiO_3$ [29], KNN-$BaTiO_3$ [30], and KNN-$AgNbO_3$ [31]. The compound $(K_{0.44}Na_{0.52}Li_{0.04})(Nb_{0.84}Ta_{0.10}Sb_{0.06})O_3$ synthesized by Saito and company, is especially interesting [32]. It is a textured material (preferential orientation of grains) that possess a high d_{33} of 416 pC/N, which is one of the highest lead-free values so far reported, and is comparable to some modified PZT ceramics. This value is initially very impressive, however, upon inspection, it is apparent that some of the enhanced property is due to a shift of the tetragonal to orthorhombic phase transition ($T_{T\text{-}O}$) to room temperature [28, 33-35]. This causes the piezoelectric properties of the material to be temperature sensitive, which is a large drawback for application purposes.

1.6.2 Bi-Based Systems

Bismuth-based compounds have been getting much attention recently, because the Bi^{3+} ion has a stereochemically active $6s^2$ lone pair of electrons just like the Pb^{2+} ion [13]. It is believed that because of this lone pair, bismuth compounds should be highly polarizable and also posses a large polarization in the same way as lead-based systems. $BiScO_3$ has been used to replace $PbZrO_3$ in PZT in an effort to reduce the amount of lead in the system. Dielectric and piezoelectric properties were enhanced due to the presence of an MPB, and a high T_C of 450°C was also reported [10, 36].

High Curie temperatures are fairly typical of Bi-based compounds, which allows for relatively temperature independent properties and a larger temperature range for the operation of the piezoelectric devices. For example, $BiFeO_3$ has a very high T_C of 850 °C [37] and $BiAlO_3$ was recently shown to have a high T_C of > 520 °C [38].

Several Bi-based systems have recently been investigated, including $Bi(Ga,Sc)O_3$-$PbTiO_3$ [39, 40], $BiInO_3$-$PbTiO_3$ [10], $BiYbO_3$-$PbTiO_3$ [10], and KNN-$BiFeO_3$ [37]. However, many bismuth compounds have low perovskite stability and limited solubility, which usually prevent the formation of MPB.

1.7 Objectives of This Work and Organization of the Thesis

The recent push for lead-free materials has opened up a large field for research in the area of solid-state ferroelectrics. Many systems have been studied and a great deal of investigation has progressed, however, all of that work simply opens more opportunities to study new systems for a better understanding of lead-free capabilities in the search for materials with high performance and a high T_C for applications, which will ultimately

replace the currently used PZT ceramics in modern technologies. Therefore, the objective of this work is to develop new synthetic methods to improve the sintering and to optimize the properties of the promising lead-free KNN solid solution systems.

In this work, we strive to improve the properties of KNN ceramics by two approaches. In the first approach, we address the poor sinterability issue. By using a sintering aid we develop a simple, cost effective technique to increase the density of the KNN ceramics, and thereby improve the properties of this material. On the other hand, in the second approach, we modify the system chemically by forming a new solid solution. By synthesizing the new lead-free (1-*x*)KNN-*x*BA solid solution, we couple the qualities of each end member synergistically in order to improve the piezoelectric and ferroelectric properties on the whole.

1.7.1 Synthesis of KNN ceramics with Fluoride Sintering Aid

As mentioned earlier, KNN has been recognized as a promising host material for new lead-free piezoelectric materials. However, the inability to sinter ceramics well by traditional solid state sintering methods presents a significant drawback. It is this sintering problem that we attempt to address in the first part of our work (**Chapter 3**).

In this work, KNN-based ceramics are prepared by solid-state synthesis using KF as a sintering aid. It was hypothesized that because KF has a lower melting point (898°C) than KNN (1140°C), it would function as an intergrain sintering agent to lower the sintering temperature of KNN, thereby improving the density of ceramics. The mixture of fluorides (LiF + MgF_2) was previously shown to effectively enhance the densification of ferroelectric $LiTaO_3$ and $LiNbO_3$ ceramics [41-43]. For this reason, the effectiveness of

KF as a sintering agent is studied. In order to investigate the sintering mechanism, chemical and physical analyses are performed by means of Energy Dispersive Spectroscopy (EDS) and X-ray Photoelectron Spectroscopy (XPS). The ceramic density, crystal structure, and dielectric, piezoelectric and ferroelectric properties are characterized using various techniques, including X-ray diffraction (XRD), dielectric spectroscopy, Scanning Electron Microscopy (SEM), and piezo-/ferroelectric measurements.

1.7.2 KNN-BA Solid Solution

A solid solution is a single phase formed from two or more different end members. Formation of solid solutions has proved to be an effective method to synthesize new piezo-/ferroelectric materials with excellent properties, in particular with the existence of an MPB. Besides the already promising KNN system, the bismuth aluminate, $BiAlO_3$ (BA), has attracted much attention recently because of its lead-free character and its high T_C [38]. Bi-based compounds are attractive due to the stereochemically active lone pair of electrons on the Bi^{3+} ion, as discussed previously. BA crystallizes in a rhombohedral structure at room temperature. However, it is difficult to synthesize BA under normal pressure. Moreover, it decomposes on heating at 547°C [38]. Therefore, incorporating BA into a solid solution is a viable alternative to stabilize BA. Baettig et al. predicted that solid solutions containing BA may potentially be high-performance piezoelectrics [44], so it would be interesting to synthesize a solid solution of BA with KNN, i.e. (1-*x*)KNN-*x*BA. It is hypothesized that the lone pair would further increase the polarizability of the KNN host material, and hopefully lead to an increase in

properties. It was also thought that, because KNN and BA adopt different symmetries at room temperature (orthorhombic and rhombohedral, respectively), an MPB may exist in the solid solution, which would enhance the dielectric and piezoelectric properties. Therefore, the second part of our work (**Chapter 4**) is dedicated to the synthesis of this new lead-free (1-*x*)KNN-xBA solid solution system in the form of ceramics, and to characterize the structure and the dielectric, piezoelectric and ferroelectric properties by means of X-ray diffraction, dielectric spectroscopy, and piezo-/ferroelectric measurements. During the progress of this work, it came to our attention that Zuo et al. reported the synthesis of the similar system [45]. However, the results described in Chapter 4 are from our independent and original work, which has been taken beyond the report of Zuo et al.

References

[1] M. E. Lines and A. M. Glass, *Principles and Applications of Ferroelectrics and Related Materials* (Clarendon Press, Oxford, 1977).

[2] Y. Xu, *Ferroelectric Materials and Their Applications* (North-Holland, Amsterdam, 1991).

[3] R. Blinc and B. Zeks, *Soft Modes in Ferroelectrics and Antiferroelectrics* (North-Holland, Amsterdam, 1974).

[4] T. Ikeda, *Fundamentals of Piezoelectricity* (Oxford University Press, New York, 1990).

[5] D. Damjanovic, Rep. Prog. Phys. **61**, 1267 (1998).

[6] J. F. Nye, *Pysical Properties of Crystals* (Oxford University Press, Oxford, 1985).

[7] G. H. Haertling, J. Am. Ceram. Soc. **82**, 797 (1999).

[8] http://americanpiezo.com/piezo_theory/.

[9] V. M. Goldschmidt, Naturwissenschaften **14**, 477 (1926).

[10] R. E. Eitel *et al*., Jpn. J. Appl. Phys. **40**, 5999 (2001).

[11] M. N. Rahaman, *Sintering of Ceramics* (CRC Press, Florida, 2008).

[12] A. R. West, *Basic Solid State Chemistry* (John Wiley & Sons, New York, 1999).

[13] R. E. Cohen, Nature (London) **358**, 136 (1992).

[14] K. D. Karlin, *Progress in Inorganic Chemistry, Vol. 51* (John Wiley & Sons, New Jersey, 2003).

[15] B. D. Begg, E. R. Vance, and J. Nowotny, J. Am. Ceram. Soc. **77,** 3186 (1994).

[16] B. Jaffe, R. S. Roth, and S. Marzullo, J. Res. Nat. Bur. Stand. **55**, 239 (1955).

[17] B. Jaffe, W. R. Cook, and H. Jaffe, *Piezoelectric Ceramics* (Academic Press, London, 1971).

[18] W. Cao and L. E. Cross, Phys. Rev. B. **47**, 4825 (1993).

[19] http://ec.europa.eu/environment/waste/index.htm.

[20] R. D. Shannon, Acta Cryst. **A32**, 751 (1976).

[21] G. H. Haertling, J. Am. Ceram. Soc. **50**, 329 (1967).

[22] R. E. Jaeger and L. Egerton, J. Am. Ceram. Soc. **45**, 209 (1962).

[23] A. Safari and E. K. Akdogan, *Piezoelectric and Acoustic Materials for Transducer Applications* (Springer, USA, 2008).

[24] M. Kosec and D. Kolar, J. Am. Ceram. Soc. **10**, 335 (1975).

[25] H. Birol, D. Damjanovic, and N. Setter, J. Eur. Ceram. Soc. **26**, 861 (2006).

[26] Y. P. Guo, K. Kakimoto, and H. Ohsato, Appl. Phys. Lett. **85**, 4121 (2004).

[27] Y. P. Guo, K. Kakimoto, and H. Ohsato, Mater. Lett. **59**, 241 (2005).

[28] G. Z. Zang *et al.*, Appl. Phys. Lett. **88**, 212908 (2006).

[29] R. Wang *et al.*, Phys. Status Solidi (a) **202**, R57 (2005).

[30] Y. Guo, K. Kakimoto, and H. Ohsato, Jpn. J. Appl. Phys. **43**, 6662 (2004).

[31] C. Lei and Z.-G. Ye, Appl. Phys. Lett. **93**, 042901 (2008).

[32] Y. Saito *et al.*, Nature (London) **432**, 84 (2004).

[33] S. J. Zhang, R. Xia, and T. R. Shrout, J. Electroceramics **19**, 251 (2007).

[34] Y. J. Dai, X. W. Zhang, and G. Y. Zhou, Appl. Phys. Lett. **90**, 262903 (2007).

[35] E. K. Akdogan *et al.*, Appl. Phys. Lett. **92**, 112908 (2008).

[36] R. E. Eitel *et al.*, Jpn. J. Appl. Phys. **41**, 2099 (2002).

[37] S. A. Fedulov, Sov. Phys.-Doklady **6**, 726 (1962).

[38] J. Zylberberg *et al.*, Chem. Mater. **19**, 6385 (2007).

[39] J. Cheng *et al.*, J. Appl. Phys. **94**, 605 (2003).

[40] S. J. Zhang *et al.*, J. Appl. Phys. **93**, 2880 (2003).

[41] Z. G. Ye, R. Von Der Muhll, J. Ravez and P. Hagenmuller, J. Mater. Res. **3,** 112 (1988).

[42] Z. G. Ye, R. Von Der Muhll, J. Ravez and P. Hagenmuller, J. Phys. Chem. Solids **49,** 1153 (1988).

[43] Z. G. Ye, R. Von Der Muhll and J. Ravez, in "Proceedings of the 1990 IEEE 7th International Symposium on Applications of Ferroelectrics (ISAF '90)", IEEE 566 (1991).

[44] P. Baettig *et al.*, Chem. Mater. **17**, 1376 (2005).

[45] R. Zuo *et al.*, J. Alloy Compd. **476**, 836 (2009).

CHAPTER 2:
Characterization: Principles and Techniques

2.1 Introduction

In this chapter, we will present the basic principles for the various experimental techniques used to investigate the structure and properties of the materials studied in this work. These techniques include chemical and structural analyses, and characterization of physical properties of the materials by dielectric, piezoelectric and ferroelectric measurements.

2.2 Powder X-ray Diffraction (XRD)

Powder x-ray diffraction (XRD) is a technique that was used to characterize the phase components, structure, phase symmetry and lattice parameters of the materials prepared in this work. In this technique, an electric field is used to accelerate electrons, which are directed at a metal target [1]. The penetrating electrons eject other electrons out of their atomic orbitals, specifically from the inner most (*K*) shell. This vacancy in the *K* shell is then filled by an electron from the closest shell higher in energy (*L*) or the one above that (*M*), yielding two sharp and intense x-ray peaks, K_α and K_β, respectively [2]. The difference in energy between the two shells is released as radiation in the form of an x-ray. Since the energies of the shells are well defined, each transition produces a monochromatic beam line.

A Rigaku Rapid-Axis x-ray diffractometer using copper K_α (λ=1.5418 Å) radiation (46 kV, 42 mA) was used to produce powder diffraction patterns in this work.

Figure 2.1 illustrates how x-rays interact with the planes in the crystal lattice of the sample. This interaction can also be expressed by the Bragg law [2]:

$$2d_{hkl}\sin\theta = \lambda \quad , \tag{2.1}$$

where d_{hkl} is the interplanar spacing between the crystal planes (*hkl*), θ is the Bragg angle at which diffraction from these planes are observed, and λ is the wavelength of the x-rays. The diffracted x-rays are detected and a plot of intensity as a function of the 2θ angle can be produced. This XRD pattern provides very useful information such as the *d*-spacing of the lattice planes, which is directly related to the unit cell parameters of the material, and the symmetry of the phase(s) present [3].

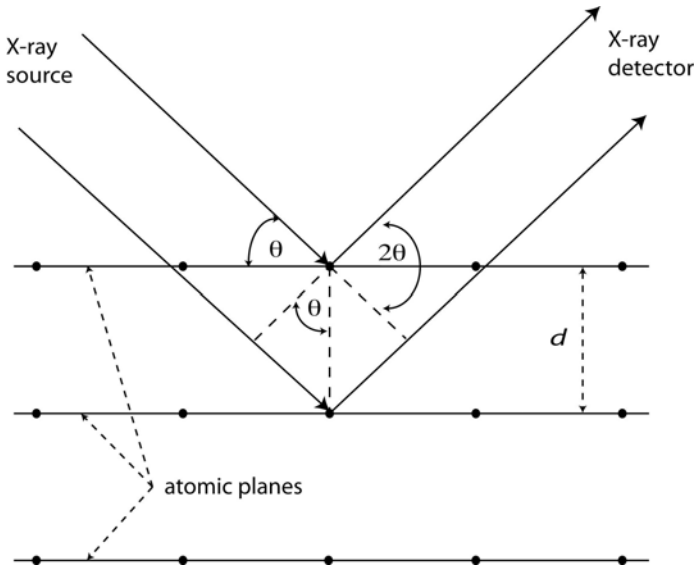

Figure 2.1: Bragg diffraction from a set of lattice planes with a spacing *d*.

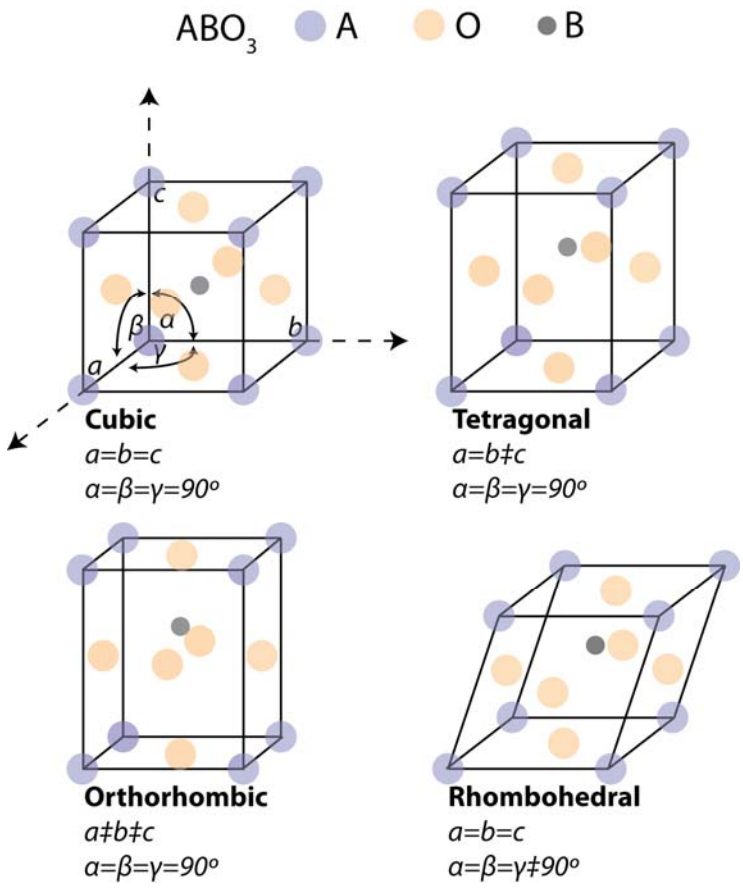

Figure 2.2: Illustration of various unit cell types with corresponding lattice parameters for a perovskite, ABO_3, structure.

A unit cell is characterized by six lattice parameters (*a, b,* and *c,* and α, β, and γ), which represent the lengths of the unit cell and the interaxial angles, respectively (Fig. 2.2). As a crystal undergoes a structural phase transition, the lattice parameters change along with *d*-spacings. Depending on the type of structure adopted by the material, the relationship between *d*-spacing and lattice parameters varies. The *d*-spacings for a material with a crystal structure of orthogonal axes, i.e. cubic, tetragonal or orthorhombic, can be expressed as follows [2]:

$$\frac{1}{d_{hkl}^2} = \frac{h^2}{a^2} + \frac{k^2}{b^2} + \frac{l^2}{c^2} \quad , \tag{2.2}$$

where *h*, *k*, and *l* are the Miller indices.

X-ray diffraction patterns can be used to monitor chemical reactions and structural properties such as phase purity and change of symmetry (phase transition). For example, if a crystal structure changes from cubic to tetragonal, the interaxial angles do not change ($\alpha, \beta, \gamma = 90°$), but the lengths of the unit cell are no longer equal ($a = b \neq c$). This will affect the *d*-spacings within the lattice, which in turn will result in the splitting or merging of peaks as shown in Figure 2.3. This characteristic XRD pattern can be used to identify the symmetry and phase components of the materials.

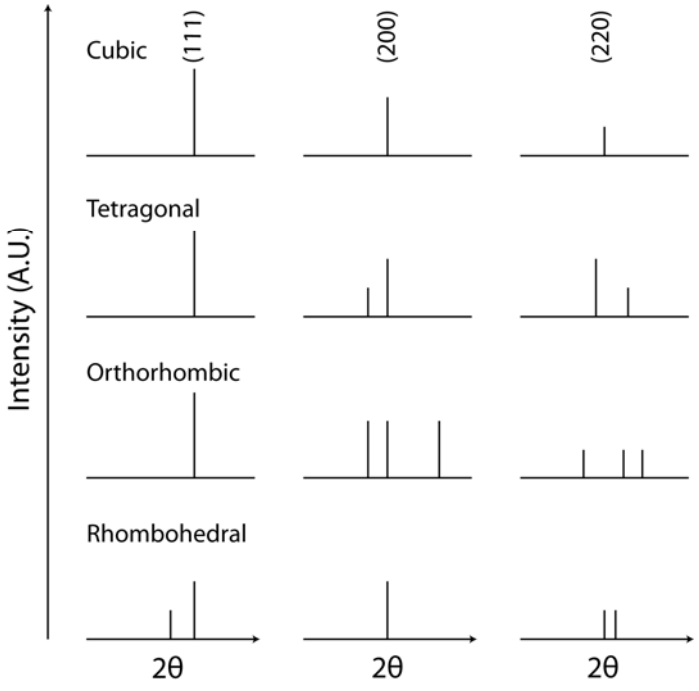

Figure 2.3: Characteristic x-ray diffraction patterns for various symmetries showing the corresponding splitting with respect to the cubic (111), (200) and (220) reflections.

2.3 Dielectric Permittivity Measurements

Dielectric property measurements allow for the determination of phase transition temperatures, permittivity values, and dielectric loss. Dielectric properties of the ceramics as a function of frequency and temperature were performed using a Solartron 1260 impedance analyzer in conjunction with a Solartron 1296 dielectric interface. The relative real permittivity, or dielectric constant (ε_r), is determined based on the following equation:

$$C = \varepsilon_r \varepsilon_o \left(\frac{A}{d} \right) \quad , \tag{2.3}$$

where C is the capacitance of the dielectric material between two parallel electrodes, ε_o is the permittivity of free space, 8.854x10^{-12} F/m, A is the area of one of the plates of the parallel electrodes, and d is the distance between them [3, 4].

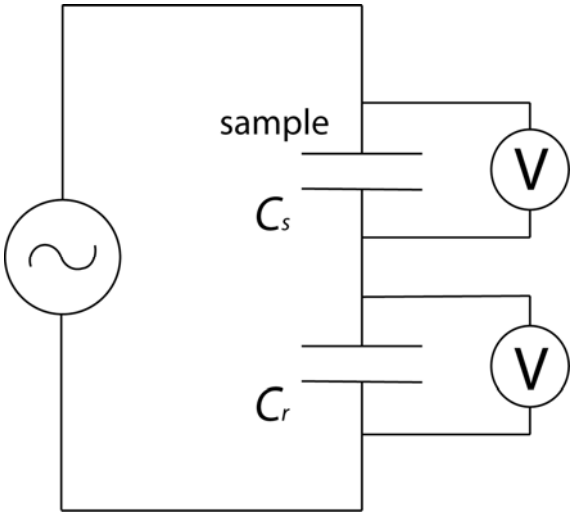

Figure 2.4: A schematic diagram of the circuit used in the dielectric permittivity measurements.

Figure 2.4 shows a schematic of the circuit used in this technique. In this circuit, the voltage is applied by a signal generator across the pair of electrodes on the surfaces of a sample capacitor (C_s, with thickness, d) and a reference capacitor (C_r). The voltage (V_r) across the reference capacitor is measured, and because the two capacitors are connected in series, the charge (Q_r) on the reference capacitor must be the same as the charge (Q_s) over the sample capacitor (Q_r=Q_s). This means that the charge on the sample can be found by:

$$Q = C_r \times V_r \quad . \tag{2.4}$$

The voltage (V_s) is also measured across the sample, allowing for the capacitance of this material to be determined by using the following equation:

$$C_s = \frac{Q}{V_s} \quad . \tag{2.5}$$

Once the capacitance of the sample (C_s) is obtained, the dielectric permittivity can be determined using Equation 2.3. The existence of dielectric loss, which may be caused by leakage current, also needs to be considered when writing the expression for permittivity. Charge with respect to current (I) can be described as:

$$Q = I \times t \quad , \tag{2.6}$$

where t is time. This expression indicates that the charge resulting from the leakage current is time dependent. Therefore, the dielectric permittivity must be expressed in complex form as a function of frequency (f) [5]:

$$\varepsilon_r^*(f) = \varepsilon'(f) - i\varepsilon''(f) \quad , \tag{2.7}$$

where ε' is the real part of the dielectric permittivity, termed the dielectric constant, $i = \sqrt{-1}$, and ε'' is the imaginary part of the dielectric permittivity. The dielectric loss is

related to the imaginary part of the permittivity, however, it is most often described by the tangent of the dielectric loss angle ($tan\delta$) [5]:

$$\tan\delta = \frac{\varepsilon''}{\varepsilon'} \quad , \tag{2.8}$$

where δ is the angle between the imaginary component and the real component of the permittivity, as illustrated in Figure 2.5. In this work the dielectric loss ($tan\delta$) and permittivity (ε') are measured as a function of temperature at various frequencies.

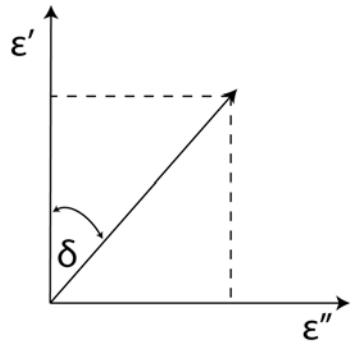

Figure 2.5: Illustration of the dielectric loss angle (δ) as a function of the imaginary and real components of the permittivity.

2.4 Ferroelectric Hysteresis Measurements

The ferroelectric properties of the ceramics prepared in this work are characterized using an RT66A Standard Ferroelectric testing system, which performs measurements of polarization as a function of electric field. Polarization (P) may be defined as:

$$P = \frac{Q}{A} \quad , \tag{2.9}$$

where Q is the charge developed on the electrodes of the ferroelectric capacitor and A is the area of the electrodes. A Sawyer-Tower circuit allows for the determination of a material's polarization as a function of electric field [6], which gives rise to a ferroelectric hysteresis loop shown in Figure 1.1 in Chapter 1.

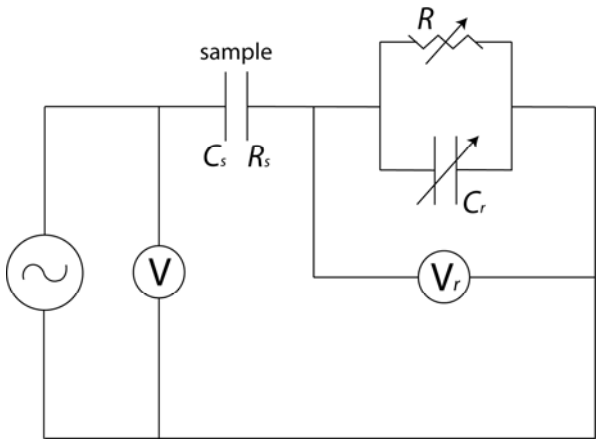

Figure 2.6: A modified Sawyer-Tower circuit for the measurement of ferroelectric hysteresis loops (adapted from Ref. [7]), where C_s, R_s, C_r, R, V, and V_r stand for the capacitance of the sample, the resistance of the sample, the capacitance of the reference, the resistor, the step voltage, and the voltage across the reference capacitor, respectively.

Figure 2.6 shows a schematic of a modified Sawyer-Tower circuit. In this circuit, a step voltage (V) is applied by the signal generator across the pair of electrodes on the surfaces of a sample capacitor (C_s, with thickness d). This is the origin of the quantity plotted on the horizontal x-axis, which is proportional to the electric field ($E=V/d$) across the sample. The sample is then connected in series with a parallel RC circuit, which compensates for any phase shift due to conductivity or dielectric loss in the sample. The voltage (V_r) across the reference capacitor (C_r) is measured, and because the two capacitors are connected in series, the charge on the reference capacitor must be the same

as the charge over the sample capacitor. This means that the charge on the ferroelectric sample can be found by using Equation 2.4, as discussed previously. Once the charge on the sample is known, the polarization can be determined using Equation 2.9 above.

As discussed in Chapter 1, the electric polarization obtained in ferroelectric hysteresis measurements arises from three contributions: the dielectric component, the domain switching component, and the leakage current contribution (Fig.1.2). Polarization with respect to current (I) can be described as:

$$P = \frac{I \times t}{A} \quad , \tag{2.10}$$

where t is time. This expression indicates that the polarization resulting from the leakage current is time dependent, therefore a relatively high frequency is used in hysteresis measurements so that the contribution from the leakage current component can be minimized to reveal the contribution from polarization (domain) reorientation and switching.

2.5 Piezoelectric Property Measurements

The piezoelectric coefficient (d_{33}) of the ceramics studied in this work was measured by a quasi-static method using a Piezo-d_{33}/d_{31} Meter (ZJ-6B). The piezoelectric coefficient is defined by the following equation:

$$d_{33} = \left(\frac{D_3}{T_3} \right)_E \quad , \tag{2.11}$$

where D_3 is the charge density (C/m^2) and T_3 is the mechanical stress (N/m^2) at constant electric field (E). Figure 2.7 shows a schematic diagram for the d_{33} measurement using the Piezo-Meter.

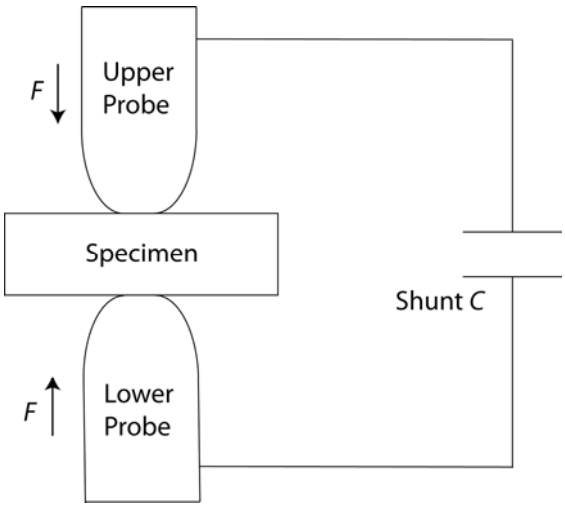

Figure 2.7: A schematic diagram for the d_{33} measurement by a quasi-static method.

When a force (F) is applied on an area (A) of a sample by the upper and lower probes, a piezoelectric charge (Q) is produced due to the piezoelectric effect on the contact area (A), therefore Equation 2.11 can be simplified at follows:

$$d_{33} = \frac{(Q/A)}{(F/A)} = \frac{Q}{F} = \frac{C \times V}{F} \quad , \tag{2.12}$$

where C is the shunt capacitance and V is the potential difference across the shunt capacitor. The Piezo-Meter measures this potential difference, calculates the d_{33} (in pC/N) of the sample and displays the value digitally. Average d_{33} values are reported after taking measurements from various areas across a ceramic sample.

Impedance measurements were also performed to determine the electromechanical coupling factor (k) using a Solartron 1260 impedance analyzer in conjunction with a Solartron 1296 dielectric interface. The electromechanical coupling factor is a measure of the efficiency of how well a piezoelectric material can convert electrical energy into mechanical energy, or vice versa [8]. Depending on the dimensions

and symmetry of the material, there are different expressions for k. A thin piezoelectric ceramic disc, like the materials prepared in this work, produces radial vibrations when exposed to an alternating electric field, which is applied parallel to the direction in which the ceramic is polarized [8]. The planar coupling factor (k_p) expresses this radial coupling by the following equation [9]:

$$k_p{}^2 = 2.5\frac{(f_a - f_r)}{f_r} \quad , \tag{2.13}$$

where f_a and f_r are the anti-resonance and resonance frequencies, respectively. The resonance frequency is the frequency at which the material vibrates most readily or where the impedance is at a minimum as seen in Figure 2.8 [8]. This is the point at which the sample most efficiently converts electrical energy into mechanical energy, and vice versa. As the frequency is further increased the impedance reaches a maximum, and it is this frequency that is termed the anti-resonance frequency. Once these two frequencies are determined for a ceramic disc, the planar coupling factor can be calculated using Equation 2.13 above.

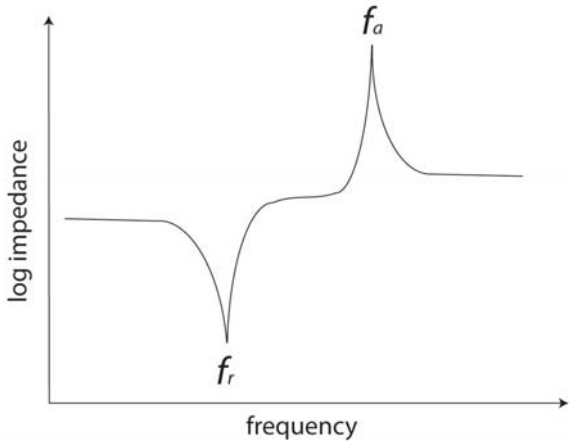

Figure 2.8: Impedance as a function of frequency, displaying resonance (f_r) and anti-resonance (f_a) frequencies.

2.6 Scanning Electron Microscopy (SEM)

The microstructures of the ceramics prepared in this work were examined by a Scanning Electron Microscope (SEM; Hitachi S-3400N). SEM is a technique that images a sample's surface enabling us to investigate the topography, structure, morphology, grain size, defects, etc., of solid materials.

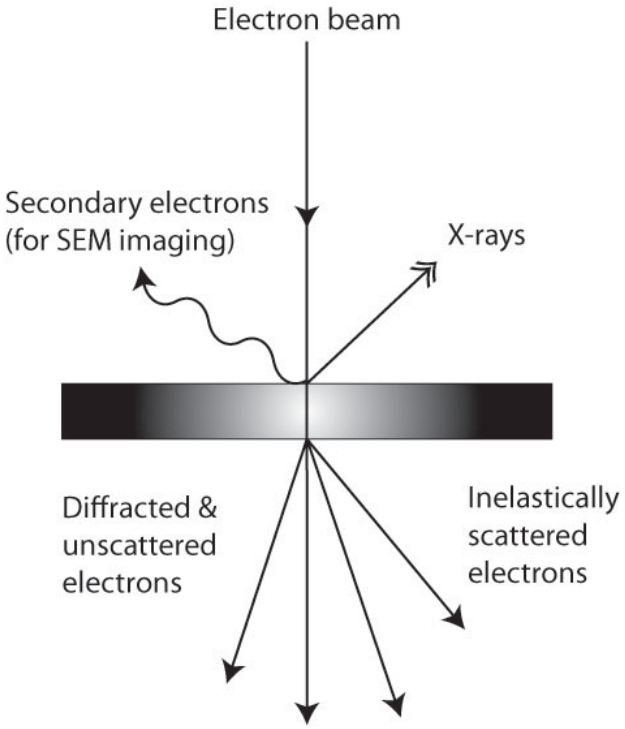

Figure 2.9: The interaction of an electron beam with a sample (adapted from Ref. [10]).

In order to image the sample's surface, an electron beam is thermally emitted from a tungsten filament under vacuum and focused on an area (< 10 nm) and then scanned across the sample (Fig. 2.9). The electrons penetrate the surface and consequently eject other electrons that are detected and used for imaging [10]. Because

electrons enter the material, the sample must be conducting, and so the ceramics in this work were coated with a sputtered gold layer for SEM studies.

2.7 Energy Dispersive Spectroscopy (EDS)

Chemical analysis of the ceramics studied in the work was performed by Energy Dispersive Spectroscopy (EDS; x-ray analyzer [EDAX] feature of the SEM; FEI DualBeam Strata 235), which is a technique used for elemental analysis of a material. In this technique, a beam of electrons is focused into the material. Atoms within the material contain ground state electrons, which reside in discrete energy levels from the nucleus. The electron beam can eject an electron from an inner shell leaving a hole, which is then filled by the descent of an electron from an outer shell or higher energy level (Fig. 2.10). The difference in energy between these two levels will then be released in the form of an x-ray and the number and energy of these x-rays can be measured by a spectrometer [11].

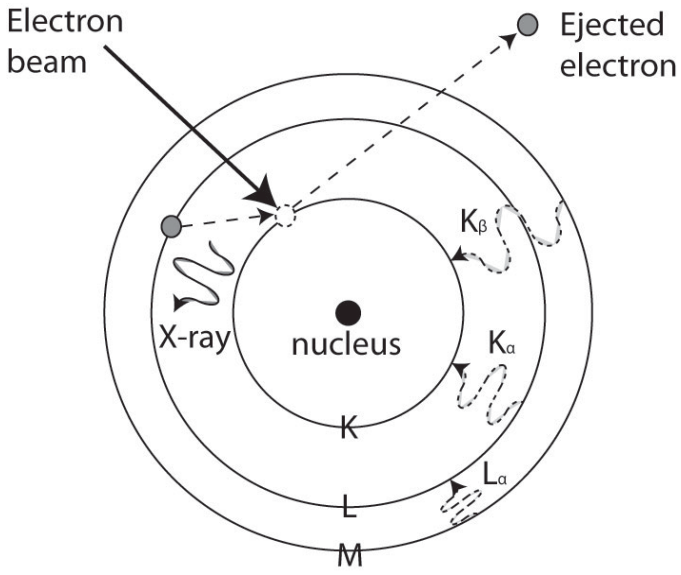

Figure 2.10: The interaction of an electron beam with electrons within an atom used in EDS.

The energies of the x-rays released are characteristic of the difference in energy levels and of the atomic structure of the element from which they were emitted, therefore the elemental make-up of a material can be determined. EDS is able to detect elements with an atomic number (Z) of 5 and above [11]. It cannot detect hydrogen (Z = 1), helium (Z = 2), lithium (Z = 3) or beryllium (Z = 4).

2.8 X-ray Photoelectron Spectroscopy (XPS)

Chemical analysis of the ceramics prepared in this work was also performed by means of X-ray Photoelectron Spectroscopy (XPS; Axis Ultra DLD), which is a quantitative technique used widely to measure the elemental composition, chemical state and electronic state of the elements that compose a material. XPS is a surface chemical analysis technique in which the surface of a material is irradiated with a beam of x-rays under ultra high vacuum that penetrate the top 1-10 nm of the material, causing electrons to be ejected from the material being analyzed (Fig. 2.11) [12].

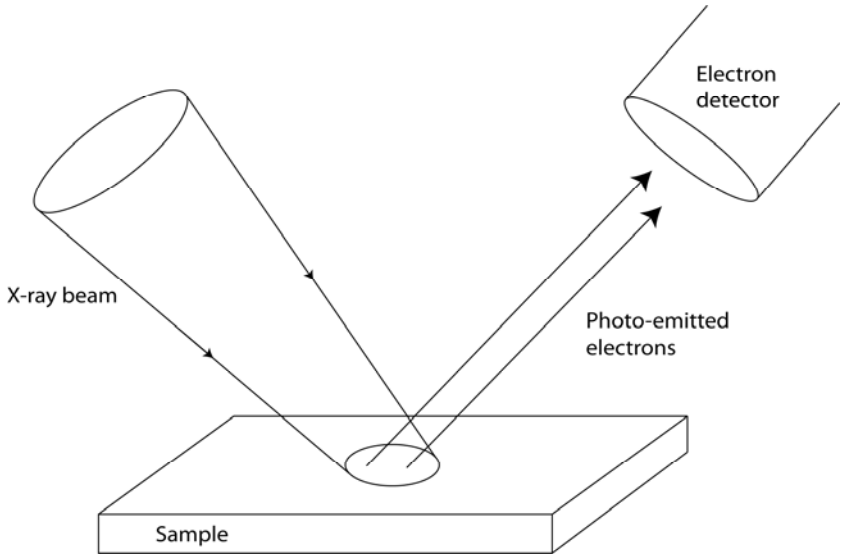

Figure 2.11: Interaction of x-rays with a specimen within the XPS setup.

XPS spectra are obtained by measuring the kinetic energy and number of electrons that escape. An XPS spectrum is a plot of electron counts versus electron binding energy (Fig. 2.12). The electron binding energy of each of the ejected electrons can be determined by using the following equation based on the early work of Rutherford:

$$E_{binding} = E_{photon} - (E_{kinetic} + \phi) \quad , \tag{2.14}$$

where $E_{binding}$ is the binding energy of an electron, E_{photon} is the energy of the x-ray photons, $E_{kinetic}$ is the kinetic energy of an electron measured by the instrument, and ϕ is the work function of the spectrometer [12]. Since the energy of a specific x-ray wavelength is known (E_{photon}), the binding energy of each electron can therefore be calculated. XPS is able to detect elements with an atomic number (Z) of 3 and above [12]. It cannot detect hydrogen (Z = 1) or helium (Z = 2). The highest detection limit for the majority of elements is approximately 100 ppm, which requires 8–16 hours of exposure time.

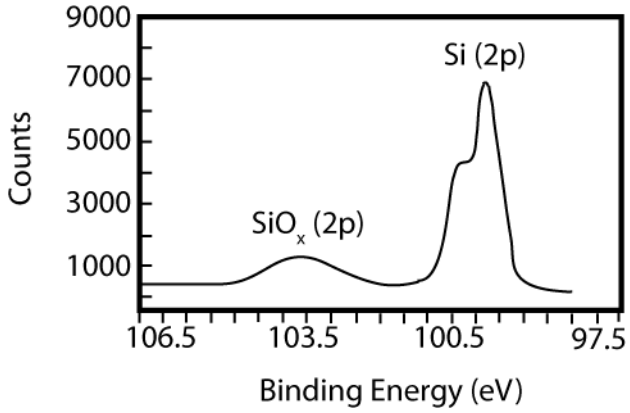

Figure 2.12: Typical XPS spectrum of a silicon wafer (adapted from Ref. [13]), showing the binding energy of a Si (2p) electron and a SiO_x (2p) electron.

References

[1] M. Ladd and R. Palmer, *Structure Determination by X-ray Crystallography* (Kluwer Academic/Plenum Publishers, New York, 2003).

[2] L. E. Smart and E. A. Moore, *Solid State Chemistry* (Taylor & Francis, London, 2005).

[3] A. R. West, *Basic Solid State Chemistry* (John Wiley & Sons, New York, 1999).

[4] E. Barsoukov and J. R. Macdonald, *Impedance Spectroscopy: Theory, Experiment, and Applications* (Wiley-Interscience, Hoboken, 2005).

[5] Y. Xu, *Ferroelectric Materials and Their Applications* (North-Holland, Amsterdam, 1991).

[6] C. B. Sawyer and C. H. Tower, Phys. Rev. **35**, 269 (1930).

[7] M. E. Lines and A. M. Glass, *Principles and Applications of Ferroelectrics and Related Materials* (Clarendon Press, Oxford, 1977).

[8] http://americanpiezo.com/piezo_theory/.

[9] T. F. Hueter, D. P. Neuhaus, and J. Kolb, J. Acous. Soc. Am. **26**, 696 (1954).

[10] A. K. Cheetham and P. Day, *Solid State Chemistry: Techniques* (Clarendon Press, Oxford, 1987).

[11] R. F. Egerton, *Physical Principles of Electron Microscopy: An Introduction to TEM, SEM, and AEM* (Springer, New York, 2005).

[12] T. L. Barr, *Modern ESCA: The Principles and Practice of X-ray Photoelectron Spectroscopy* (CRC Press, Boca Raton, 1994).

[13] http://en.wikipedia.org/wiki/X-ray_photoelectron_spectroscopy.

CHAPTER 3:
Preparation and Characterization of KNN-Type Piezo- and Ferroelectric Ceramics by a New Sintering Process

3.1 Abstract

Lead-free ceramics based on the $(K_{0.5}Na_{0.5})NbO_3$ (KNN) solid solution are known to display promising piezoelectric properties. However, it is difficult to obtain dense ceramics of KNN by conventional sintering methods. In this work KNN-based ceramics have been prepared by a new solid-state synthetic method using KF as a sintering agent. The addition of KF resulted in dense ceramics with a relative density reaching 92% after sintering at 1120 °C. By varying the amount of KF used in the sintering process, it was found that the KNN ceramics sintered with 0.5% KF displayed the best piezoelectric properties. The piezoelectric coefficient (d_{33}), planar electromechanical coupling factor (k_p), and dielectric loss tangent were found to be 125 pC/N, 0.38, and 0.025, respectively, at room temperature. These properties represent an improvement over those of conventionally sintered KNN ceramics. The SEM imaging revealed that the ceramics sintered with KF were less porous than the KNN ceramics. This enhanced densification correlates well with the improved electrical properties. The Curie temperature (T_C) was unaffected by the addition of KF and remains high at 420 ^oC, which indicates that KF was not incorporated into the perovskite structure of KNN. Chemical analyses were performed by means of energy dispersive spectroscopy (EDS) and x-ray photoelectron spectroscopy (XPS) to deduce the sintering mechanism, and the results confirm that the fluoride indeed acted as a sintering agent without entering the lattice of KNN.

3.2 Introduction

Ferroelectric materials exhibit a spontaneous and switchable polarization and large dielectric constants as a result of their high polarizability, which make them useful for such applications as in memory devices and capacitors [1, 2]. The non-centrosymmetric and polar structure of these materials below a certain Curie temperature (T_C), which is specific to each material [1], implies a loss of inversion center, causing ferroelectric materials to also exhibit piezoelectric properties, furthering applications for use in sensors, actuators or high voltage generators [1]. A high T_C is therefore desired in order to have the largest possible operation range of these materials.

Currently, lead containing materials, such as $Pb(Zr_{1-x}Ti_x)O_3$ and $(Pb_{1-y}La_y)(Zr_{1-x}Ti_x)O_3$, exhibit the best ferro-/piezoelectric ceramic properties [1]. However, lead is toxic both environmentally and biologically, which has encouraged the scientific community to develop lead-free alternatives. Unfortunately, the availability of lead-free systems is limited considering the requirement for materials with good piezoelectric performance and a high T_C. To date, one of the most interesting families of materials is the $(1-x)KNbO_3$-$xNaNbO_3$ (KNN) solid solution-based ceramics [1, 3, 4]. KNN crystallizes in a perovskite structure with orthorhombic symmetry and has a high T_C of 420 °C. When the composition is at 50% of each end member, the solid solution exhibits a morphotropic phase boundary (MPB), which defines the boundary between two phases, where the material shows enhanced electrical properties [1, 3]. These characteristics of KNN make it a promising candidate as a lead-free piezoelectric material; however, it is difficult to obtain dense ceramics of KNN by conventional sintering methods due to its high hygroscopicity and the volatility of K_2O at high temperatures during sintering, which

inevitably changes the stoichiometry [3, 5, 6]. Hot-pressing method has proven to increase the density and properties of KNN ceramics [3. 6], however, this route is more expensive than conventional sintering and requires specialized equipment.

In this work, KNN-based ceramics were prepared by a novel solid-state synthetic technique using KF as a sintering aid. It was hypothesized that because KF has a lower melting point (898 °C) it would function as an inter-grain flux to lower the sintering temperature of KNN, thereby improving the density of the ceramics. The mixture of fluorides (LiF + MgF_2) was previously shown to effectively enhance the densification of ferroelectric $LiTaO_3$ and $LiNbO_3$ ceramics, the mechanism of which involves the formation and disappearance of a transient intermediate phase of $Mg_4Ta_2O_9$-type [7-9]. For this reason, the effectiveness of KF as a sintering agent of KNN ceramics was studied. Chemical analyses were also performed in order to investigate the sintering mechanism.

3.3 Experimental Procedure

Ceramic samples of $(K_{0.5}Na_{0.5})NbO_3$ + *x* mole% KF, with *x* = 0, 0.5, 1, 2 and 5, were prepared using solid-state reaction. Stoichiometric amounts of K_2CO_3, $Na_2CO_3{\cdot}H_2O$, and Nb_2O_5 powders were mixed together and hand-ground for one hour in acetone. The mixtures were calcined at 800 °C for 4 hours and then reground in acetone for one hour with the addition of *x* mole% KF and polyvinylalcohol (6% PVA solution) (one drop per gram of powder) as binder. Finally, these powders were pressed into 10 mm-diameter pellets of 2-5 mm thickness by means of uniaxial pressing. The pellets were

heated up to 600 °C in a muffle furnace for one hour to drive off the PVA binder, and then sintered at a temperature of 1120 °C for 4 hours in air.

The density of the ceramics was determined by measuring the volume and mass of each pellet. X-ray powder diffraction (XRD) patterns were recorded on a Rigaku Rapid Axis x-ray diffractometer using Cu $K\alpha$ radiation (46 kV, 42 mA) and were used to characterize the phase components and lattice parameters of the sintered ceramics. The microstructures of the ceramics were observed using a Hitachi S-3400N Scanning Electron Microscope (SEM). Chemical analysis was performed in order to detect the presence of any fluorine using Energy Dispersive Spectroscopy (EDS) provided by the x-ray analyzer [EDAX] feature of the SEM, and X-Ray Photoelectron Spectroscopy (XPS) (Axis Ultra DLD). To measure the dielectric and piezoelectric properties, the ceramics were polished to give parallel and flat surfaces, and Au electrodes were sputtered onto the opposite sides of each pellet. Complex dielectric properties ,

$$\varepsilon^* = \varepsilon' + i\varepsilon'' \quad , \tag{1}$$

where ε*, ε' and ε'' are the complex, real and imaginary permittivities, respectively, were measured using a Solartron 1260 impedance analyzer in conjunction with a Solartron 1296 dielectric interface upon cooling from 550 °C to 25 °C in the measurement frequency range of 100 Hz to 1 MHz. These samples were then poled using a Stanton PS350 high voltage power source at 30 kV/cm in silicon oil for 10 minutes in a Delta 9023 variable temperature chamber at 130 °C. The piezoelectric coefficient, d_{33}, was measured using a ZJ-6B Quasistatic d_{31}/d_{33} Meter (Chinese Academy of Sciences). The planar electromechanical coupling factor (k_P) was calculated based on resonance and

anti-resonance frequencies that were measured using the same equipment as used above for dielectric measurements, according to the following equation [10]:

$$k_P{}^2 = 2.5\frac{(f_a - f_r)}{f_r} \quad , \tag{2}$$

where f_r and f_a are the resonance and anti-resonance frequencies corresponding to the minimum and maximum of the impedance spectrum, respectively.

3.4 Results and Discussion

3.4.1 Densification of the Ceramics

Synthesis of KNN using potassium fluoride (KF) as a sintering agent was found to produce dense ceramics. Figure 3.1 gives the variation of the relative density of the ceramics as a function of content of the fluoride additive. It shows a dramatic increase in the relative density (based on the theoretical density of 4.51 g/cm^3 [6]) of ceramics upon a small addition of KF, with the ceramic sintered with 0.5 mole % KF showing the largest relative density of 92% (± 0.05%).

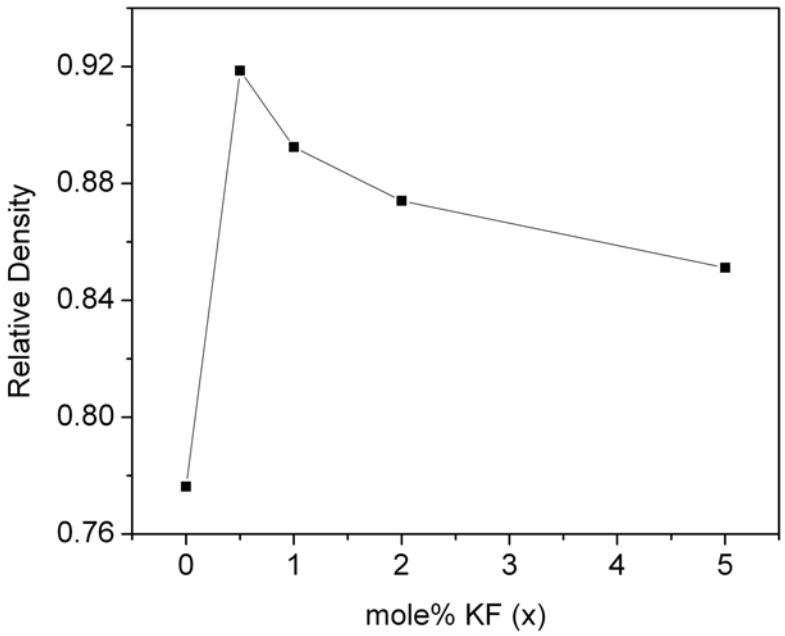

Figure 3.1: Relative density of KNN ceramics as a function of mole% KF, sintered at 1120 °C for 4 hours.

3.4.2 Phase Analysis by X-Ray Diffraction

X-ray diffraction (XRD) patterns of KNN sintered with various amounts of KF as the sintering agent show that the ceramics obtained are of pure perovskite phase with an orthorhombic symmetry (Bmm2) [11] (Fig. 3.2).

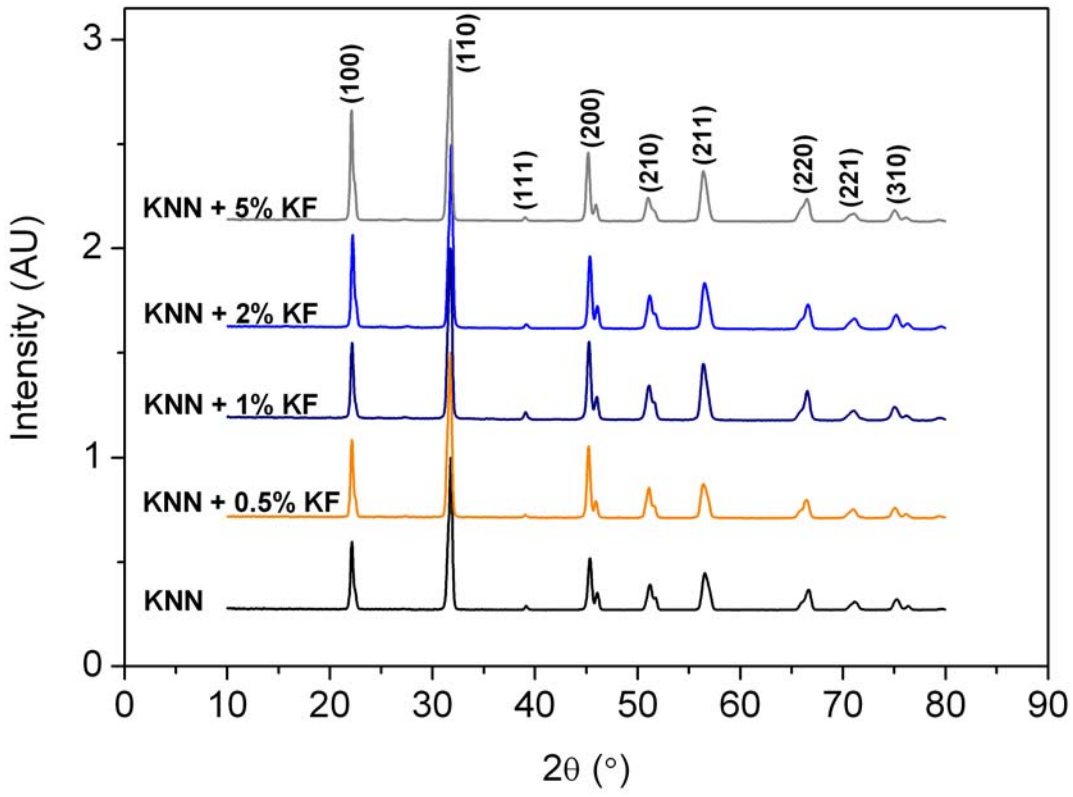

Figure 3.2: XRD patterns of KNN ceramics sintered with various mole% KF, sintered at 1120 °C for 4 hours.

The XRD patterns were also used to determine the lattice parameters, which are shown in Figure 3.3. It can be seen that the lattice parameters remain relatively constant with the addition of up to 5 mole% KF (Fig. 3). The constant lattice dimensions suggest that the fluoride was not incorporated into the perovskite structure. The radius of the fluoride anion (1.33Å [12]) is smaller than the radius of the oxygen anion (1.4Å [12]), so the lattice parameters would have decreased if fluoride had in fact entered the KNN lattice. In addition, the substitution of F^- for O^{2-} would require reduction of a cation in order to balance the charge, which seems to be unlikely in air.

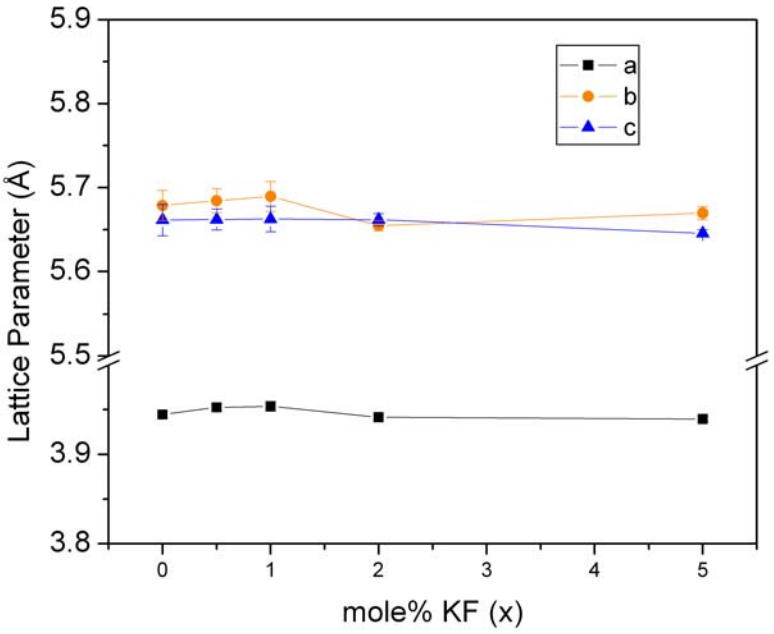

Figure 3.3: Lattice parameters (*a*, *b*, *c*) as a function of % KF sintering aid for ceramics sintered at 1120 °C for 4 hours.

3.4.3 Dielectric Properties

The variation of the dielectric constant (ε') of the KNN ceramics as a function of temperature is shown in Figure 3.4. It can be seen that the Curie temperature (T_C) of the ferroelectric to paraelectric phase transition in KNN is unaffected by the use of KF as a sintering aid regardless of the amount added, and it remains high at 420 °C. This is a very promising advantage, which ensures a wide operation temperature range for the KNN ceramics synthesized.

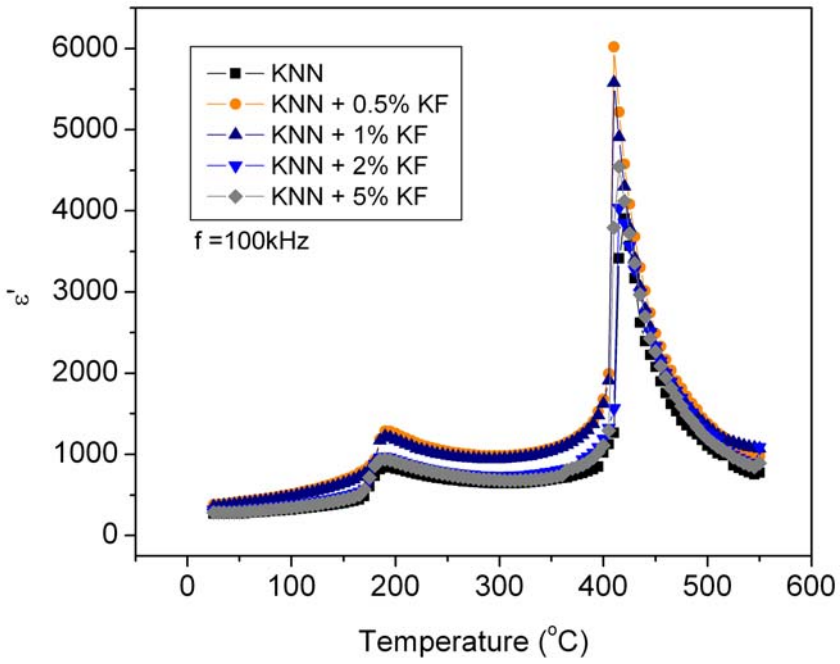

Figure 3.4: Temperature dependence of the dielectric constant (ε') of the KNN ceramics sintered with various mole% KF (x).

It is also interesting to note from this plot that the tetragonal to orthorhombic phase transition temperature ($T_{T\text{-}O}$), that occurs at 200 °C, is also unaffected by the KF-aided sintering. This is the second indication that fluoride did not enter the KNN lattice. Otherwise, the maxima in the $\varepsilon'(T)$ curves, which indicate the T_C and $T_{T\text{-}O}$, would have been affected by the change in the composition of the ceramics and would have shifted on the temperature axis. These two phase transitions can also be observed in the plot of dielectric loss tangent ($tan\delta$), which is a measure of energy dissipation, as a function of temperature (Fig. 3.5).

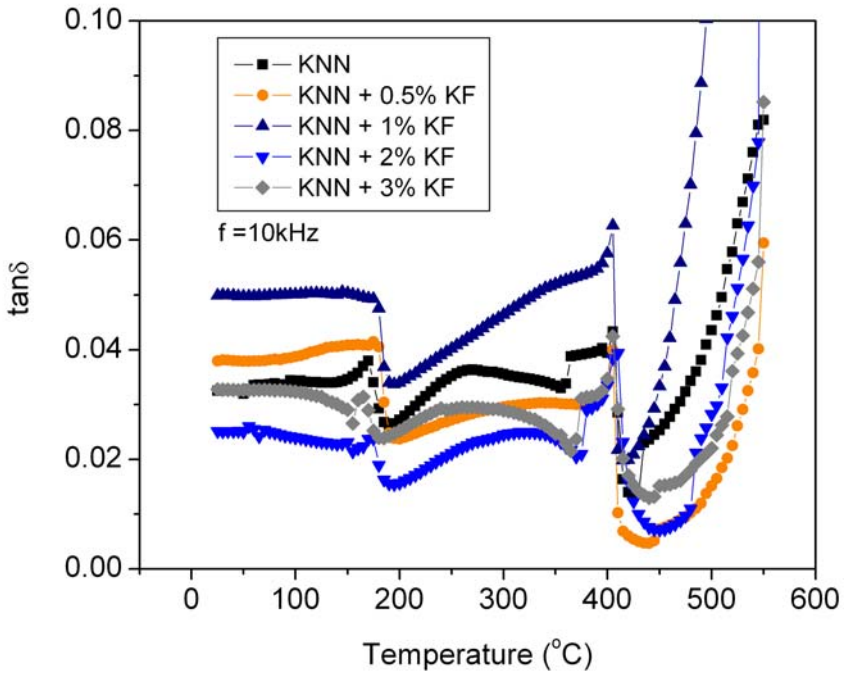

Figure 3.5: Temperature dependence of the loss tangent of the KNN ceramics sintered with various mole% KF (*x*).

A sharp peak in the $tan\delta$ vs. temperature curve represents the T_C and a local maximum occurs at the $T_{T\text{-}O}$, which correlates well with permittivity data. It is also observed that the dielectric losses remain below 0.06 over a large temperature range (25-500 °C) despite the initial addition of KF.

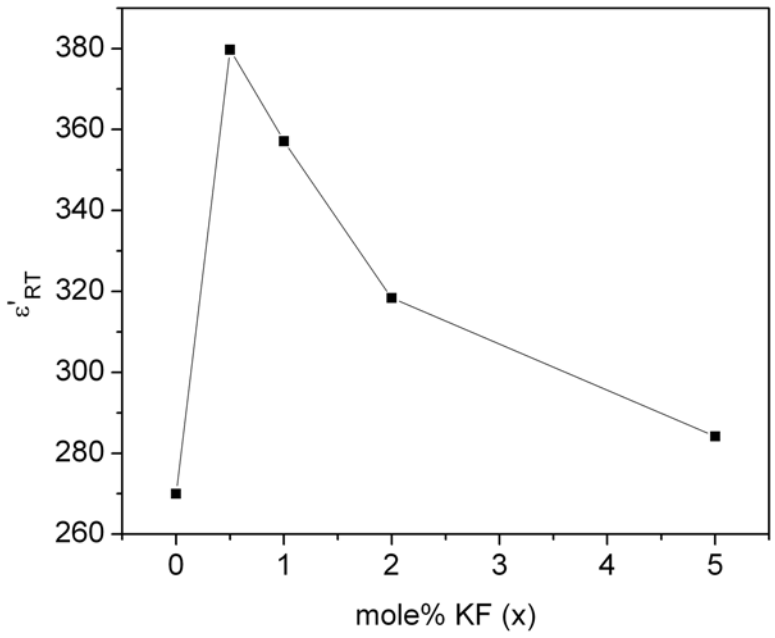

Figure 3.6: Composition dependence of the room temperature dielectric permittivity (ε'_{RT}) of the KNN ceramics sintered with various mole% KF (x).

The room temperature permittivity (ε'_{RT}) values were plotted against mole % KF, and are presented in Figure 3.6. All ceramics sintered with KF show higher room temperature permittivity values than those of pure KNN (ε'_{RT} = 270), with the KNN ceramic sintered with 0.5 mole% KF having the largest value (ε'_{RT} = 380). The piezoelectric charge coefficient (d_{ij}) is directly related to the relative permittivity according to [13, 14]:

$$d_{ij} \sim 2Q_{ij} \times K \times \varepsilon_o \times P_i \quad , \tag{2}$$

where Q_{ij}, K, ε_o, and P_i are the electrostrictive coefficient, relative permittivity, the permittivity of free space, and the remnant polarization after poling, respectively. Therefore, considering negligible changes in the electrostrictive coefficient, as the room temperature permittivity increases, the piezoelectric charge coefficient will also increase.

Based on Figure 3.5, it is expected that the KNN ceramics sintered with KF have higher d_{33} values than the pure KNN ceramics, and the ceramic sintered with 0.5% KF should exhibit the largest d_{33} value.

3.4.3 Piezoelectric Characterization

The measured piezoelectric properties for the KNN ceramics prepared using five different sintering conditions are shown in Figure 3.7. It is found that the trend in the piezoelectric properties vs. mole% KF relation correlates well with the variation of density vs. mole% KF. As the density increases, so do the piezoelectric properties. Having an improved density (d = 4.143 g/cm^3) over that of pure KNN (d = 3.501 g/cm^3), the ceramic sintered with 0.5% KF indeed shows the best piezoelectric properties with a piezoelectric coefficient (d_{33}) of 125 pC/N and a planar electromechanical coupling factor (k_P) of 38%. This trend is validated because a ceramic that is less porous (one that is more dense) is expected to have a larger permittivity thus a higher piezoelectric charge coefficient since the relative dielectric permittivity of air has a value of $\varepsilon_r = 1$.

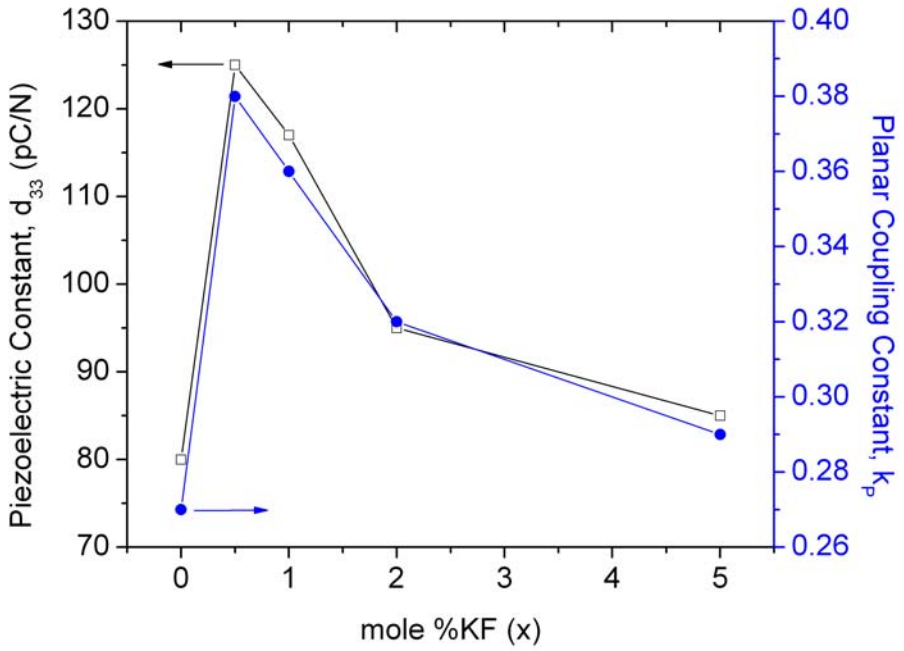

Figure 3.7: Variation of the piezoelectric coefficient (d_{33}) and planar electromechanical coupling factor (k_P) for the KNN ceramics sintered with various mole% KF (x).

Recently, several other studies on KNN-based systems were reported with enhanced d_{33} values, such as KNN-Li (7%) (d_{33} = 240 pC/N) [15], $(K_{0.44}Na_{0.52}Li_{0.04})(Nb_{0.86}Ta_{0.10}Sb_{0.}04)O_3$ (KNN-LF4, textured) (d_{33} = 410 pC/n) [4, 16], and KNN-SrTiO3 (d_{33} = 200 pC/N) [17, 18]. However it should be pointed out in each of these systems the phase transition at $T_{T\text{-}O}$ was shifted close to room temperature (at 20, 25 and 27 °C, respectively) as a result of the chemical substitutions. This polymorphic effect was the true reason for the increase in the observed piezoelectric properties. This $T_{T\text{-}O}$ phase transition results in an increase in permittivity at room temperature, which as explained earlier, gives rise to higher d_{33} values, since the piezoelectric coefficient is measured at room temperature as well. The issue rising from this shift of $T_{T\text{-}O}$ to room

temperature is the temperature instability of the piezoelectric properties, which is a severe issue for these materials to be used in devices especially at high temperatures. In contrast, we have found a synthetic method that results in enhanced piezoelectric properties without shifting the $T_{T\text{-}O}$ phase transition at all. This means that piezoelectric performance can be maintained in a wide temperature range up to T_{RT}/T_C, a feature that is very important for practical applications.

3.4.4 Microstructure Analysis

SEM images were taken of the ceramics sintered with 0, 0.5, 1, 2 and 5% KF (Fig. 3.8). It is clear that all samples sintered with KF are less porous than pure KNN. The 0.5% KF-sintered sample is confirmed to exhibit the most dense microstructure, which again correlates well with the enhanced electrical properties.

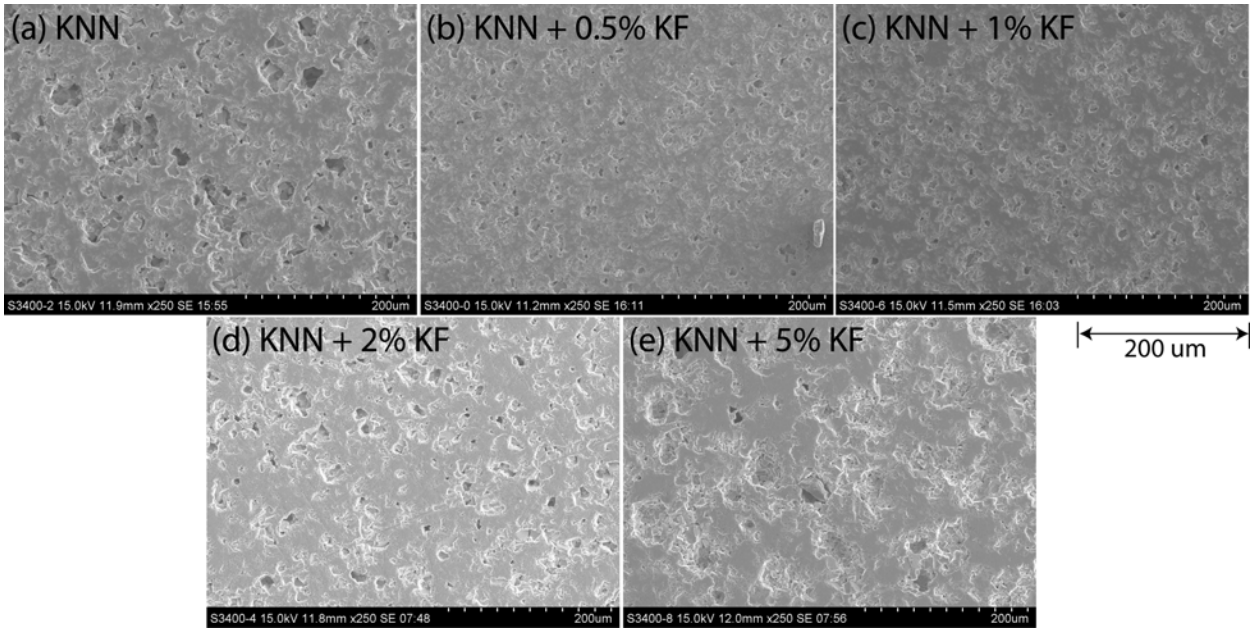

Figure 3.8: SEM images of the KNN ceramics sintered with various mole% KF (*x*) at 1120 °C for 4 hours.

3.4.6 Sintering Mechanism

The sintering mechanism was investigated by means of chemical analyses. Pure KNN and KNN ceramics sintered with 5 mole% KF were analyzed by EDS. If KF is incorporated into the perovskite structure of KNN, fluoride is expected to be seen within the grain. On the other hand, if it simply serves as an inter-grain sintering aid and is not incorporated into the crystal lattice, then it may be detected at the grain boundaries. Based on these reasonings, data were taken from both inside the grain and at the grain boundary.

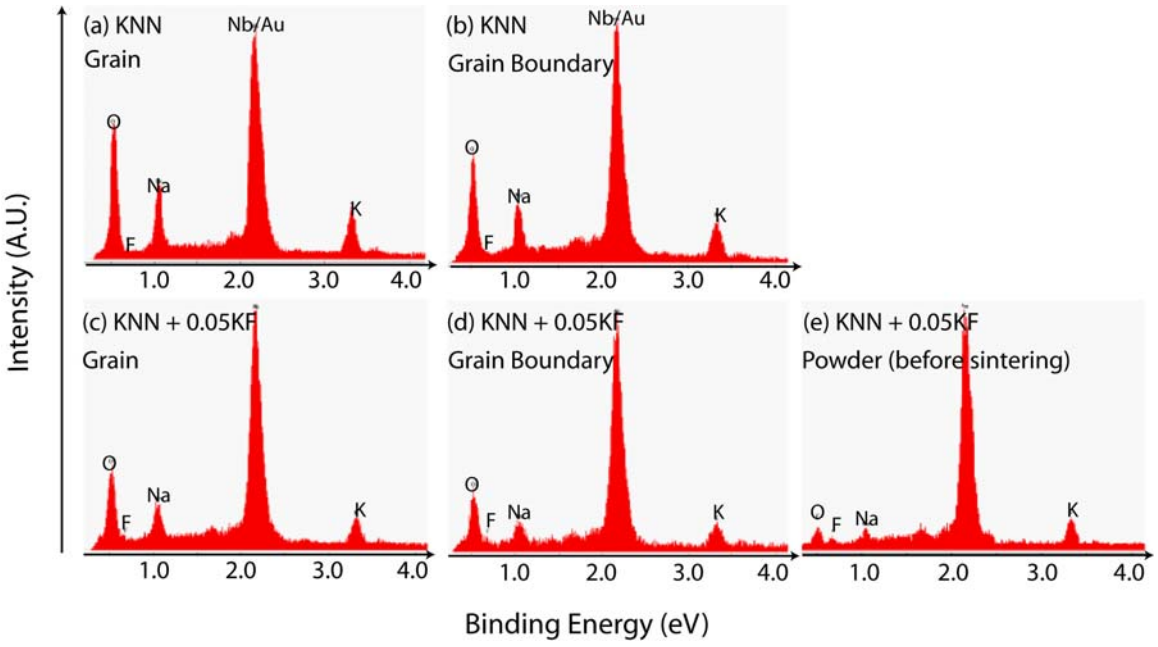

Figure 3.9: EDS spectra of (a,b) a sintered KNN ceramic, (c,d) a KNN ceramic sintered with 5 mole% KF, and (e) an unsintered (KNN + 5 mole% KF) powder (mixture).

Figure 3.9 shows the EDS spectra of (a,b) a sintered KNN ceramic, (c,d) a KNN ceramic sintered with 5 mole% KF, and (e) an unsintered (KNN + 5 mole% KF) powder

(mixture). No fluoride peak is observed either inside the grain or at the grain boundary. It was a concern, however, that the fluorine peak might be hidden beneath the oxygen peak because the energy of the core bands of fluorine is very close to that of oxygen [19]. In an attempt to resolve this uncertainty, a heterogeneous powder sample consisting of a mixture of KNN and KF powders was also analyzed before sintering. This sample contained KF and the fluorine peak is indeed clearly observed (Fig. 3.9(e)). Since this fluorine peak is seen separately from the adjacent oxygen peak, the spectra obtained from the sintered samples indicate that no fluoride is present in the final ceramics.

In order to verify these results, XPS was performed as well. Figure 3.10 shows the XPS data for (a) pure KNN, (b) KNN sintered with 3 mole% KF, and (c) KNN powder with 3 mole% KF powder.

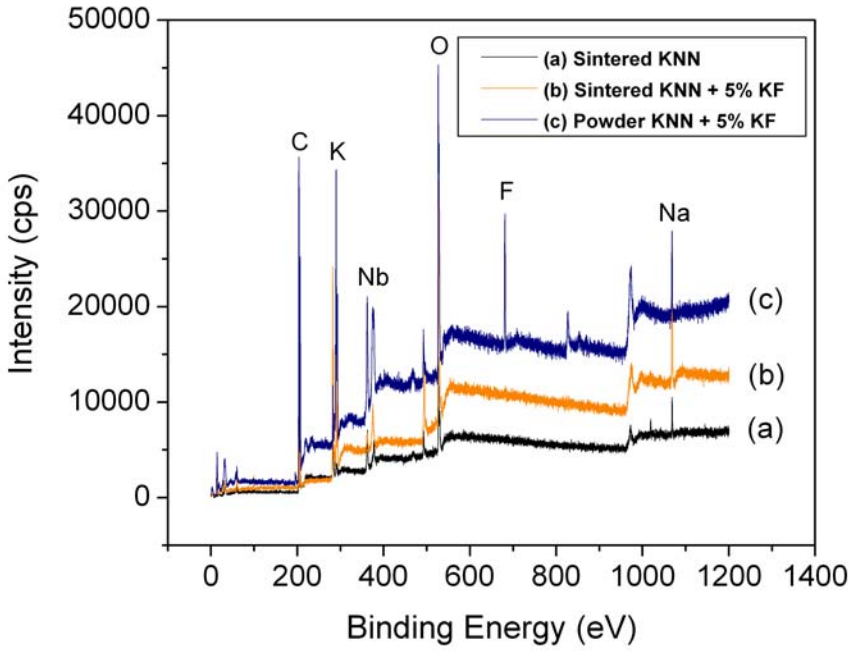

Figure 3.10: XPS spectra of (a) a sintered KNN ceramic, (b) a KNN ceramic sintered with 3 mole% KF, and (c) an unsintered (KNN + 3 mole% KF) powder (mixture).

The powder mixture (c) shows a large fluorine peak at 681 eV, whereas the two sintered samples do not show any evidence that fluoride is present. With all these results combined, it can be concluded that KF has not been incorporated into the KNN lattice of the sintered ceramics. These results, however, do not explain what was happening to the fluoride during the sintering process. Although it is clear that the fluoride is no longer present after the entire sintering process has taken place, it is unclear at what point the fluoride evaporated, so further experiments were performed to investigate the sintering mechanism.

A series of KNN pellets with 5% KF were placed into a muffle furnace individually, and heated by the original sintering profile. Then the pellets were each quenched in air to room temperature, from different temperatures of 820 °C, 920 °C, 1020 °C, 1120 °C and 1120 °C after 4 hours, respectively. These pellets were examined by XRD to monitor the presence of fluoride, if any (Fig. 3.11).

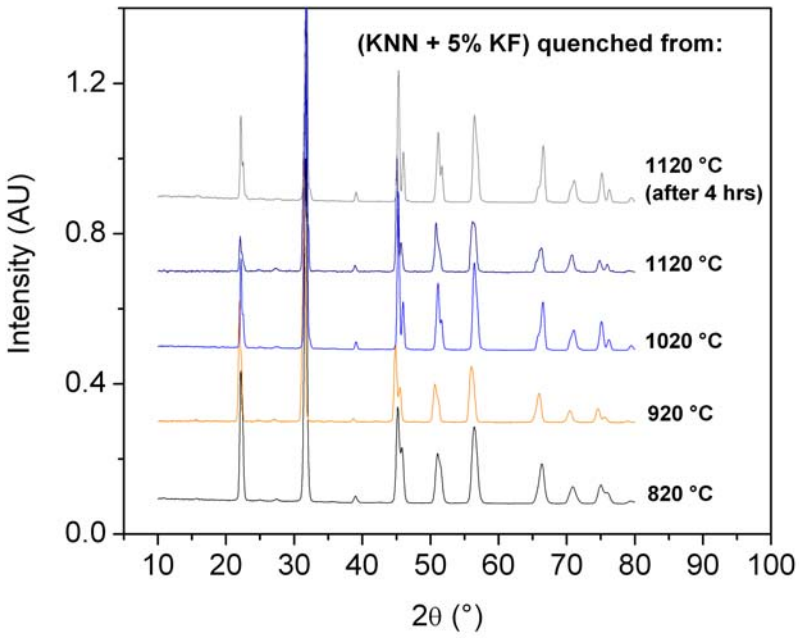

Figure 3.11: XRD patterns of (KNN + 5 mole% KF) pellets quenched from various temperatures.

All the pellets, regardless of quenching temperature, possess the pure perovskite phase, without indication of any impurity peaks that would have risen from the fluoride or fluoride-type phases. To eliminate the doubt that fluoride might still exist in small amount that would be beyond the XRD detection limit, XPS data were collected as well since the XPS measurements have already been shown to be a viable technique for the detection of trace amounts of fluoride.

The XPS data were collected from both the top surface and the cross section of the pellet in order to fully track the evolution and evaporation of the fluoride. Figure 3.12 presents XPS spectra obtained for the pellets quenched from various temperatures. The scale is set to focus attention on the area in which the fluoride peaks were observed.

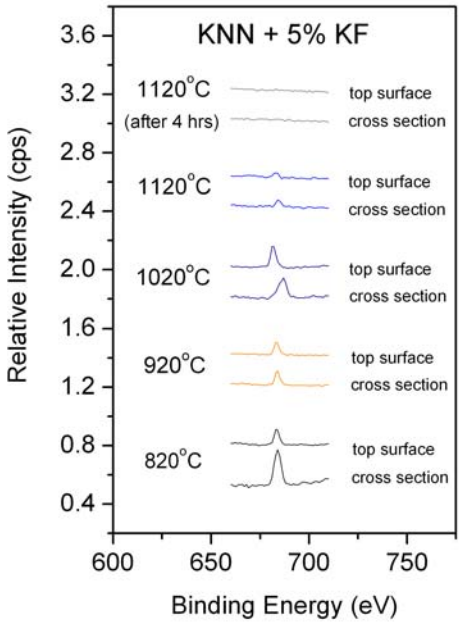

Figure 3.12: XPS spectra of (KNN + 5 mole% KF) pellets quenched from various temperatures. The spectra were taken from both the top surface and the cross section of each pellet.

It can be seen that the fluoride remains throughout the entire sample upon heating all the way up to the final sintering temperature of 1120 °C, but during the 4 hours soaking period held at this temperature, the fluoride has evaporated completely, indicating that no fluoride subsists in the sintered KNN ceramics. This is consistent with the XRD result about the absence of fluoride in the sample quenched at 1120 °C after 4 hours.

It can be concluded that during the sintering process, KF is not incorporated into the perovskite structure of KNN. Consequently, the mechanism of the sintering is proposed as follows. In order to aid in the sintering process KF partially dissolves KNN at the grain boundaries, forming a transient liquid phase that allows for and promotes migration of ions. This enhanced ionic migration causes KNN grains to grow larger, filling the pore space of the material, and finally resulting in ceramics of much higher

density than pure KNN. At the end of the sintering process, at 1120 °C for 4 hours, the fluoride has evaporated, leaving a pure perovskite oxide phase for the KNN ceramics.

3.5 Conclusions

Potassium fluoride (KF) has been successfully used as a sintering agent to produce dense ceramics of KNN. The relative density of the KNN ceramics reaches 92% following a KF-assisted sintering at 1120 °C for 4 hours. XRD, EDS, and XPS were used to investigate the sintering mechanism. It is found that fluoride is not incorporated into the KNN structure of the final ceramics, but it forms a transient liquid phase at the grain boundaries, which promotes grain growth and thereby the densification of the ceramics. The fluoride has completely evaporated in the final stages of the sintering process, giving rise to the KNN ceramics of pure perovskite oxide phase. Dielectric and piezoelectric properties of the KNN ceramics were characterized. Interestingly, the Curie temperature is not affected by KF-sintering, and it remains high at 420 °C for all the sintered samples. The KNN ceramics sintered with 0.5% KF were found to exhibit the best piezoelectric properties (d_{33} = 125 pC/N, k_P = 38%). This enhancement in the dielectric and piezoelectric properties arises directly from the enhancement in the density of the ceramics, which is achieved by the KF-assisted sintering process. Compared with currently used sintering methods such as hot-pressing and texturing, which are complex and expensive, the KF-aided sintering is shown to be a simple, inexpensive and effective technique, which can be used to produce dense KNN-based ceramics with improved dielectric and piezoelectric properties potentially useful for applications in a wide temperature operation range.

References

[1] G. H. Haertling, J. Am. Ceram. Soc. **82**, 797 (1999).

[2] D. Damjanovic, Rep. Prog. Phys. **61**, 1267 (1998).

[3] R. E. Jaeger and L. Egerton, J. Am. Ceram. Soc. **45**, 209 (1962).

[4] Y. Saito, H. Takao, T. Tani, T. Nonoyama, K. Takatori, T. Homma, T. Nagaya and M. Nakamura, Nature (London) **432**, 84 (2004).

[5] H. Birol, D. Damjanovic, and N. Setter, J. Eur. Ceram. Soc. **26**, 861 (2006).

[6] M. Kosec and D. Kolar, J. Am. Ceram. Soc. **10**, 335 (1975).

[7] Z.-G. Ye, R. Von Der Muhll, J. Ravez and P. Hagenmuller, J. Mater. Res. **3,** 112 (1988).

[8] Z.-G. Ye, R. Von Der Muhll, J. Ravez and P. Hagenmuller, J. Phys. Chem. Solids **49,** 1153 (1988).

[9] Z.-G. Ye, R. Von Der Muhll and J. Ravez, in "Proceedings of the 1990 IEEE 7th International Symposium on Applications of Ferroelectrics (ISAF '90)", IEEE 566 (1991).

[10] T. F. Hueter, D. P. Neuhaus, and J. Kolb, J. Acous. Soc. Am. **26**, 696 (1954).

[11] A. Safari and E. K. Akdogan, Piezoelectric and Acoustic Materials for Transducer Applications (Springer, USA, 2008).

[12] R. D. Shannon, Acta Cryst. **A32**, 751 (1976).

[13] S. E. Park and T. Shrout, IEEE Trans. Ultrason. Ferroelectr. Freq. Control **44**, (1997).

[14] T. R. Shrout, R. Eitel, and C. Randall, Piezoelectric Materials in Devices, ed. by N. Setter (EPFL Swiss Federal Institute of Technology, Lausanne, Switzerland, 2002), p. 413

[15] E. Hollenstein, M. Davis, D. Damjanovic and N. Setter, Appl. Phys. Lett. **87**, 182905 (2005).

[16] S. B. Lang, W. Zhu and L. E. Cross, Ferroelectrics **336,** 15 (2006).

[17] R. Wang, R. Xie, K. Hanada, K. Matsusaki, H. Bando and M. Itoh, Phys. Status Solidi A, Appl. Res. **202** R57 (2005).

[18] R. Wang, R. J. Xie, K. Hanada, K. Matsusaki, H. Bando, T. Sekiya and M. Itoh, Ferroelectrics **336,** 39 (2006).

[19] NIST X-ray Photoelectron Spectroscopy Database, Version 3.5 (National Institute of Standards and Technology, Gaithersburg, 2003); http://srdata.nist.gov/xps/.

CHAPTER 4:
Synthesis and Characterization of Lead-Free Ferroelectric Solid-Solution System $K_{0.5}Na_{0.5}NbO_3$-$BiAlO_3$

4.1 Abstract

The lead-free ferroelectric solid-solution of $(1-x)(K_{0.5}Na_{0.5})NbO_3$-$xBiAlO_3$ (KNN-BA) (x = 0 - 0.07) has been synthesized by a solid state reaction method. A pure perovskite phase was formed for compositions of $x \leq 0.02$. X-ray diffraction patterns show a transformation from an orthorhombic symmetry (with the Amm2 space group) into a pseudo-cubic symmetry as a result of the substitutions of Bi^{3+} for $(K_{0.5}Na_{0.5})^{+}$ on the *A*-site and Al^{3+} for Nb^{5+} on the *B*-site in the crystal structure of KNN. The addition of BA induces a morphotropic phase boundary between the orthorhombic phase and the pseudo-cubic phase in the composition range of $0.002 \leq x \leq 0.005$. The relative densities of the solid solution ceramics are significantly improved compared to pure KNN ceramics, with the relative density reaching as high as 96.7% for x = 0.02. The temperature dependence of the dielectric constant of the KNN-BA ceramics exhibits an increased broadening of the dielectric peaks as the BA concentration increases, indicating that the structural phase transitions in KNN become more diffuse. Large frequency dispersion is also found in the dielectric peaks, which is attributed to an increased polar disorder as a result of the addition of Bi^{3+} and Al^{3+} cations. The room temperature dielectric constant increases significantly and reaches a maximum value of 704 at x = 0.01, which is more than twice as large as the value of KNN ceramics. This can be associated with the improved density of the ceramics on the one hand, and the substitution of polar Bi^{3+} ion for $(K_{0.5}Na_{0.5})^{+}$ on the other hand. The remnant polarization

and coercive field of KNN are increased and it was not possible to obtain saturated *P*-*E* loops for the compositions of $x = 0.005$, 0.01, and 0.02. A partial phase diagram of the (1-*x*)KNN-*x*BA solid solution with $x = 0$ - 0.02 is established. The improved dielectric properties of the KNN-BA ceramics make them useful for high-energy-density capacitors.

4.2 Introduction

Lead-containing ferroelectric materials, such as $Pb(Zr_{1-x}Ti_x)O_3$ (PZT), $(Pb_{1-y}La_y)(Zr_{1-x}Ti_x)O_3$ (PLZT), and $(1-x)Pb(Mg_{1/3}Nb_{2/3})O_3$-$xPbTiO_3$ (PMN-PT), exhibit the best ferro-/piezoelectric properties in the forms of ceramics and thin films (with a relatively high T_C), which are being used in a wide range of applications as electromechanical sensors and actuators, and multilayered capacitors for energy storage. This high piezoelectric performance is attributed to the formation of a morphotropic phase boundary (MPB) bridging the rhombohedral and tetragonal phases [1, 2]. However, the toxicity of lead is of great concern, therefore, development of lead-free, environmentally friendly materials is in high demand for commercial applications of piezo-/ferroelectric materials. Potassium sodium niobate, $(K_{0.5}Na_{0.5})NbO_3$ (KNN), a compound of the MPB composition within the $(1-x)KNbO_3$-$xNaNbO_3$ solid solution, is one of the most promising lead-free (host) materials [3, 4]. KNN crystallizes in a perovskite structure with orthorhombic symmetry (space group Amm2) at room temperature, where it exhibits a reasonably high piezoelectric coefficient (d_{33} = 80 pC/N), and it has a high Curie temperature (T_C) of 420 °C. However, as mentioned in Chapter 3, it is difficult to obtain dense ceramics of KNN by conventional sintering methods due to

its high hygroscopicity and the volatility of K_2O at high temperatures during sintering, which changes the stoichiometry [3, 5, 6]. Hot-pressing methods have proven to increase the density and piezoelectric properties of KNN ceramics (with d_{33} = 160 pC/N and k_P = 45%) [3, 6], however, this route is less attractive than the conventional sintering process because it requires specialized equipment, causing it to be more expensive. A great deal of work has recently been carried out in order to improve the density and properties of the KNN-based solid solutions, such as KNN-$LiNbO_3$ [7], KNN-$LiTaO_3$ [8], KNN-$LiSbO_3$ [9], KNN-$SrTiO_3$ [10], KNN-$BaTiO_3$ [11], and KNN-$AgNbO_3$ [12].

Recent characterization of bismuth aluminate, $BiAlO_3$ (BA), ceramics synthesized under high pressure, showed that BA crystallizes in a rhombohedral structure (with a predicted R3c space group [13]) and is ferroelectric with a high Curie temperature T_C > 520 °C [14]. Its dielectric and ferroelectric properties are comparable to those of other lead-free materials, such as $BiFeO_3$ and $SrBi_2Ta_2O_9$, which makes it a promising material for memory applications [14]. Although pure BA must be synthesized by a high-pressure method, it is possible to stabilize the compound by forming a solid solution. Recent work from our laboratory has shown that BA can be incorporated into other perovskite materials to form solid solutions, such as $BaTiO_3$-BA (BT-BA) [15] and $(Na_{0.5}Bi_{0.5})TiO_3$-BA (NBT-BA) [16], in which the stable BT or NBT end member provides a host to partially stabilize BA, which in turn modifies the structure and improves the properties of the host material. Because both BA and KNN crystallize in the perovskite (ABO_3) structure, but adopt different symmetries at room temperature, an MPB is expected to form in the solid solution, which would result in enhanced properties. In this work, the lead-free (1-x)KNN-xBA solid solution has been synthesized in the form of ceramics by

the solid state reaction method, and the compositional dependences of the structure and the dielectric and ferroelectric properties have been systematically studied.

4.3 Experimental Procedure

Ceramics of the (1-*x*)KNN-*x*BA solid solution, with x = 0, 0.002, 0.005, 0.01, 0.02, 0.05 and 0.07, were prepared using the conventional solid state reaction technique. Stoichiometric amounts of K_2CO_3, $Na_2CO_3 \cdot H_2O$, Nb_2O_5, Bi_2O_3, and Al_2O_3 powders were mixed together and hand-ground for one hour in acetone. The mixtures were calcined at 800 °C for 4 hours and then reground in acetone for one hour with the addition of polyvinylalcohol (6% PVA solution) (one drop per gram of powder) as binder. Finally, these powders were pressed into 10 mm-diameter pellets of 2-5 mm thickness by means of uniaxial pressing. The pellets were heated up to 600 °C in a muffle furnace for one hour to drive off the PVA binder, and then sintered at a temperature of 1090 - 1140 °C (depending on the composition, higher temperatures were used for larger values of *x*) for 4 hours in air.

The density of the ceramics was determined by measuring the volume and mass of each pellet. X-ray powder diffraction (XRD) patterns were recorded on a Rigaku Rapid Axis x-ray diffractometer using Cu $K\alpha$ radiation (46 kV, 42 mA) and were used to characterize the phase components of the sintered ceramics. To measure the dielectric and piezoelectric properties, the ceramics were polished to give parallel and flat surfaces, and gold electrodes were sputtered onto the opposite sides of each pellet. The dielectric permittivity (ε') and dielectric loss ($tan\delta$) were determined by measuring the complex dielectric permittivity (ε^*),

$$\varepsilon^* = \varepsilon' + i\varepsilon'' \quad , \tag{1}$$

where ε' and ε'' are the real and imaginary parts, respectively, using a Solartron 1260 impedance analyzer in conjunction with a Solartron 1296 dielectric interface upon cooling from 550 °C to 25 °C in the measurement frequency range of 100 Hz to 1 MHz. Ferroelectric hysteresis measurements were performed using an RT66A Standard Ferroelectric Testing System. These samples were then poled at 30 kV/cm (using a Stanton PS350 high voltage power source) in silicon oil for 10 minutes in a Delta 9023 variable temperature chamber at 200 °C, and then cooled to room temperature with the field applied. The piezoelectric coefficient, d_{33}, was measured using a ZJ-6B Quasistatic d_{31}/d_{33} Meter.

4.4 Results and Discussion

4.4.1 Phase Analysis by X-Ray Diffraction

X-ray diffraction (XRD) patterns of the (1-x)KNN-xBA (x = 0, 0.002, 0.005, 0.01, 0.02, 0.05 and 0.07) solid solution ceramics are presented in Figure 4.1. It can be seen that all the samples with $x \leq 0.02$ exhibit a pure perovskite phase, indicating the formation of the $(K_{0.5}Na_{0.5})_{1-x}Bi_xNb_{1-x}Al_xO_3$ solid solution. Some weak peaks were observed for $x \geq 0.05$ at 2θ = 28 and 47 °, which arise from the formation of a small amount of a bismuth-deficient $Bi_2Al_4O_9$-type secondary phase. The appearance of this impurity phase indicates that the limit of solubility of BA into the KNN structural lattice is at $x \approx 0.04$. This relatively low solubility is most likely due to the chemical instability of BA under ambient pressure.

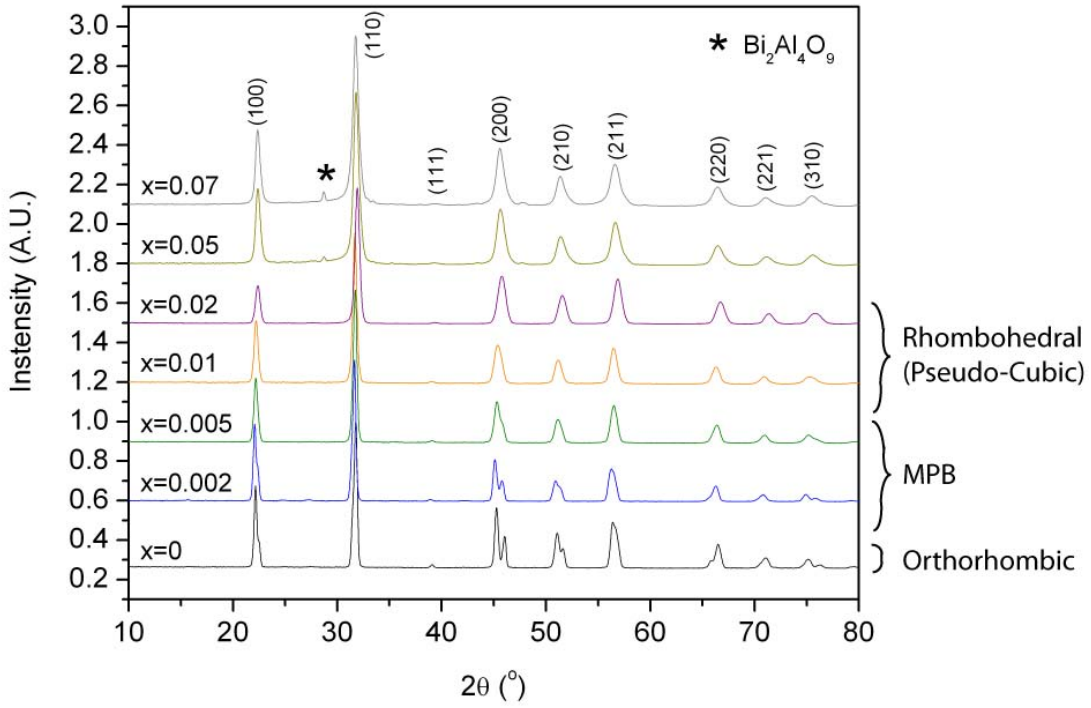

Figure 4.1: XRD patterns of the (1-*x*)KNN-*x*BA solid solution ceramics (*x* = 0, 0.002, 0.005, 0.01, 0.02, 0.05 and 0.07).

Careful analysis of the XRD patterns in Figure 4.1 reveals that the KNN-BA solid solution with low BA content ($x < 0.002$) exhibits an orthorhombic structure of KNN nature, while the compounds with a higher BA content ($x \geq 0.01$) shows a rhombohedral (or pseudo-cubic) structure of BA nature. The transformation from the orthorhombic phase of pure KNN to a rhombohedral (pseudo-cubic) phase occurs as the BA content increases and can be observed as the (200) peak, which is originally split, merges into a single peak with increasing BA content. A morphotropic phase boundary (MPB) must be present in the composition range of $0.002 \leq x \leq 0.005$, which bridges these two phases.

4.4.2 Sintering and Densification of the Ceramics

Synthesis of the solid solution (1-*x*)KNN-*x*BA, with *x* = 0, 0.002, 0.005, 0.01, and 0.02, produced ceramics that were much more dense than pure KNN ceramics. Figure 4.2 gives the variation of the relative density of the ceramics as a function of the BA content.

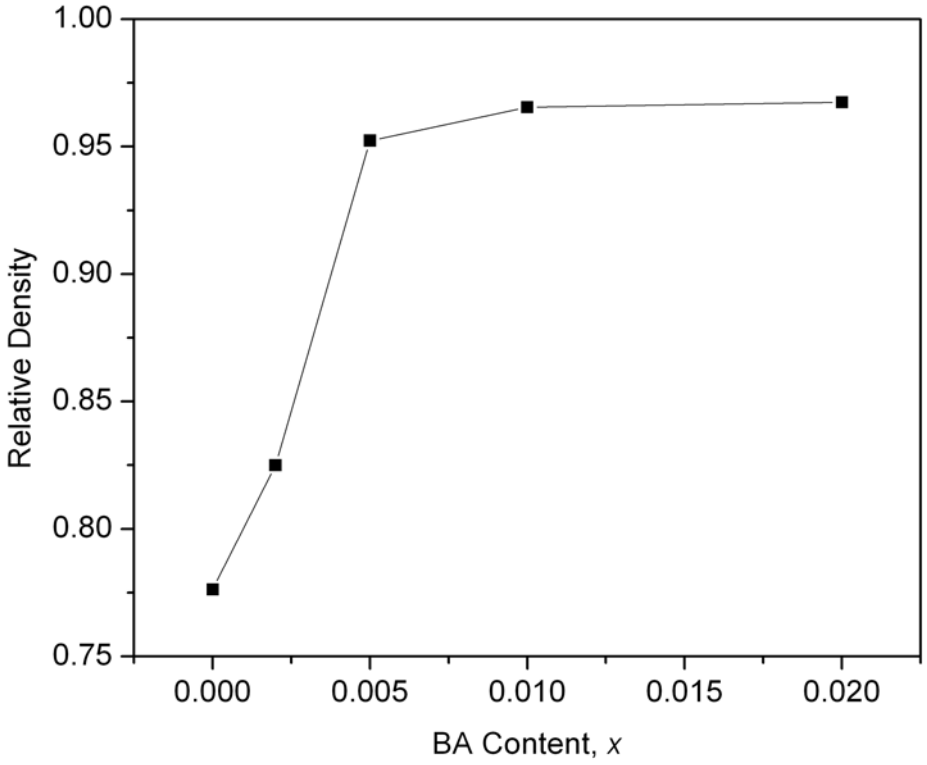

Figure 4.2: Relative density of the (1-*x*)KNN-*x*BA solid solution ceramics as a function of BA content (*x*), sintered at 1090-1140 ^{o}C for 4 hours.

It shows a dramatic increase in the relative density over pure KNN (based on the theoretical density of 4.51 g/cm^3 [17]). The density increases with increasing *x*, and the ceramic with *x* = 0.02 reaches a maximum relative density of 96.7% (errors are ± 0.05%). This result shows that $BiAlO_3$ is an effective compound that helps improve the

densification of the KNN-based ceramics. According to the temperature-composition phase diagram for Bi_2O_3-Al_2O_3 [18], a eutectic point exists at 820 ^oC, at which a liquid-type phase is formed. KNN has a relatively high melting point of 1140 ^oC, so it is reasonable to expect that a eutectic melting will take place in the multi component system of KNN-Bi_2O_3-Al_2O_3 at a lower temperature. Therefore, we hypothesize that the sintering mechanism of the (1-*x*)KNN-*x*BA ceramics involves a transient liquid phase, which promotes ionic mobility, and thereby, the grain growth and the reduction of pore volume. This liquid phase also acts as a lubricant, allowing grains to 'slide' closer together mechanically, thus increasing the density of ceramics.

4.4.3 Dielectric Properties

4.4.3.1 Frequency and Temperature Dependences of Dielectric Properties

The variations of the dielectric constant (ε') and dielectric loss ($tan\delta$) of the KNN ceramic as a function of temperature are shown in Figure 4.3(a). It can be seen that the Curie temperature (T_C) of the ferroelectric (orthorhombic) to paraelectric (cubic) phase transition occurs at a high temperature of 420 °C and the ferroelectric tetragonal to ferroelectric orthorhombic phase transition temperature (T_1) occurs at 190 °C. These two phase transitions are also manifested in the plot of dielectric loss tangent ($tan\delta$), which is a measure of energy dissipation, as a function of temperature (Fig. 4.3(f)). A sharp peak in the $tan\delta$ vs. temperature curve represents the T_C and a local maximum occurs at the T_1, which correlates well with the permittivity data for the KNN ceramics.

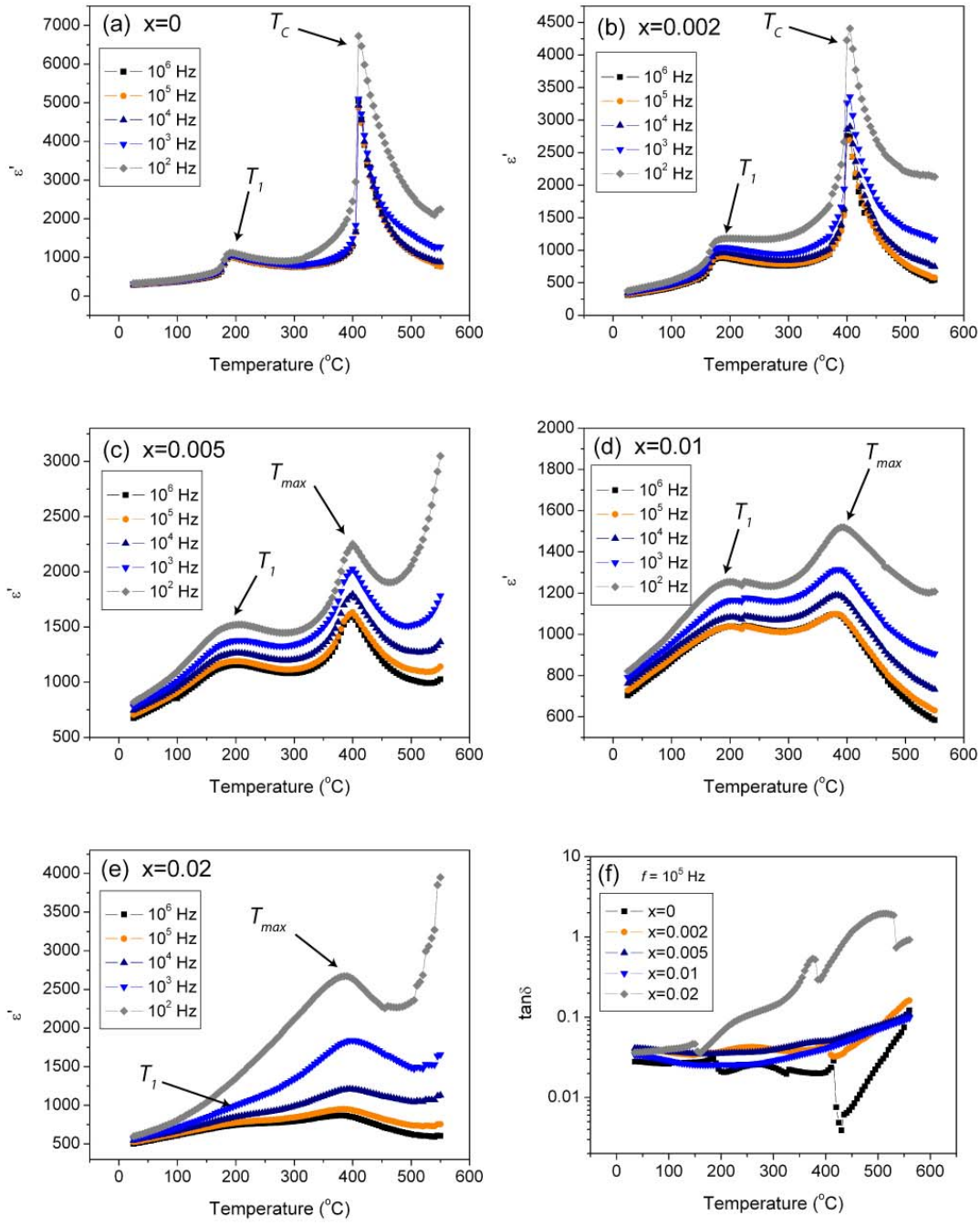

Figure 4.3: Temperature dependences of the dielectric constant and the loss tangent of the (1-*x*)KNN-*x*BA solid solution ceramics (*x* = 0, 0.002, 0.005, 0.01 and 0.02), where T_C and T_1 are the original ferroelectric (orthorhombic)/ paraelectric (cubic) phase transition and the ferroelectric (orthorhombic)/ ferroelectric (tetragonal) phase transition, respectively, and T_{max} is the maximum permittivity temperature.

The temperature dependences of ε' and $tan\delta$ of the $(K_{0.5}Na_{0.5})_{1-x}Bi_xNb_{1-x}Al_xO_3$ ceramics are shown in Figure 4.3(b-f). The temperatures of maximum permittivity (T_{max} or T_C) and T_1, have been affected by the change in the composition of the ceramics, which is another indication of the formation of the solid solution. The T_{max} decreases slightly with increasing x, while T_1 remains fairly constant up to $x = 0.01$. For $x = 0.02$, T_1 decreases in temperature (these changes will be illustrated more clearly in Section 4.4.4). Interestingly, an increased broadening of the T_{max} and T_1 peaks is observed with increasing x, which is similar to the behaviour observed in the $(Na_{0.5}Bi_{0.5})TiO_3$-$BiAlO_3$ solid solution [16], indicating that the structural phase transitions in KNN become more diffuse. In fact, T_1 becomes so diffuse for $x = 0.02$ that it almost disappears. The permittivity maxima decrease significantly when $x > 0.002$ (see Fig. 4.7 for more details) and large frequency dispersion is also found in the dielectric behaviour of these ceramics.

4.4.3.2 Structural Origins of Diffuse Phase Transitions and Dielectric Dispersion

The diffuse phase transition and dielectric dispersion can be attributed to an increased chemical disorder by the addition of Bi^{3+} and Al^{3+} into the KNN crystal lattice. The *A*-site of KNN is shared by the K^+ and Na^+ ions, and the structure is found to be disordered because XRD patterns do not show superlattice peaks that would indicate a doubling of the normal unit cell as a result of ordering. Although KNN is disordered, the valence of K^+ and Na^+ is still the same, so the polar order is not greatly affected. The *A*-site cations in KNN (K^+ and Na^+), both having the same charge, maintain the charge balance homogeneously throughout the entire material. Each dipole moment within a single unit cell interacts with dipoles in neighboring unit cells, leading to large areas, in

which all dipoles are aligned in the same direction, and the formation of ferroelectric domains. Consequently, a single macroscopic polarization direction (P) is present within each domain, as shown in Figure 4.5(a) (Figure 4.4(a-c) illustrates how (a) the 3-D perovskite structure can be projected in 2-D (b) with oxygen ions, and (c) without oxygen ions, as many of the explanations are conveniently described using 2-D projections).

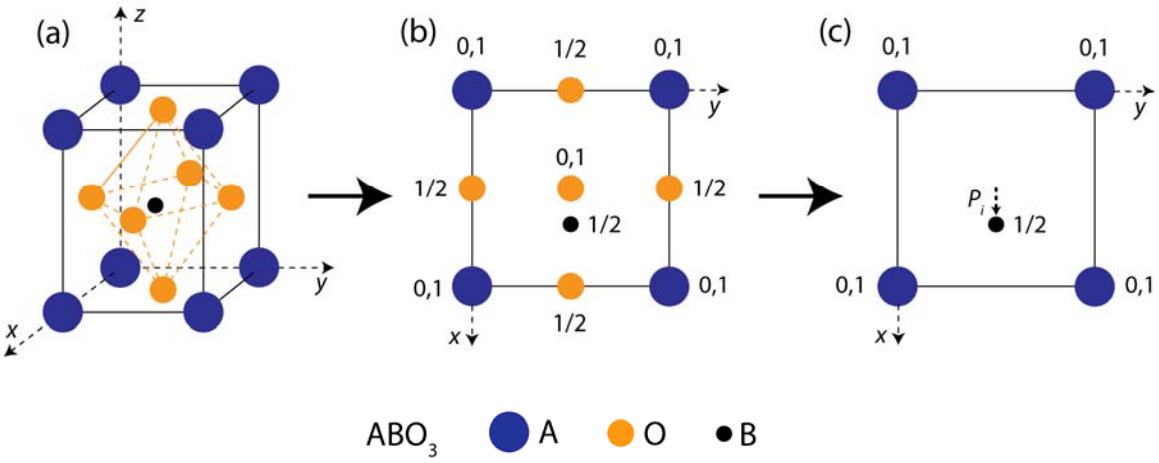

Figure 4.4: The perovskite (ABO_3) structure represented: (a) in 3-D, (b) as a 2-D projection on *x*-*y* plane, and (c) as a 2-D projection without oxygen ions (the numbers beside each ion correspond to the coordinate along *z*-axis, and P_i in (c) indicates the dipole of a unit cell).

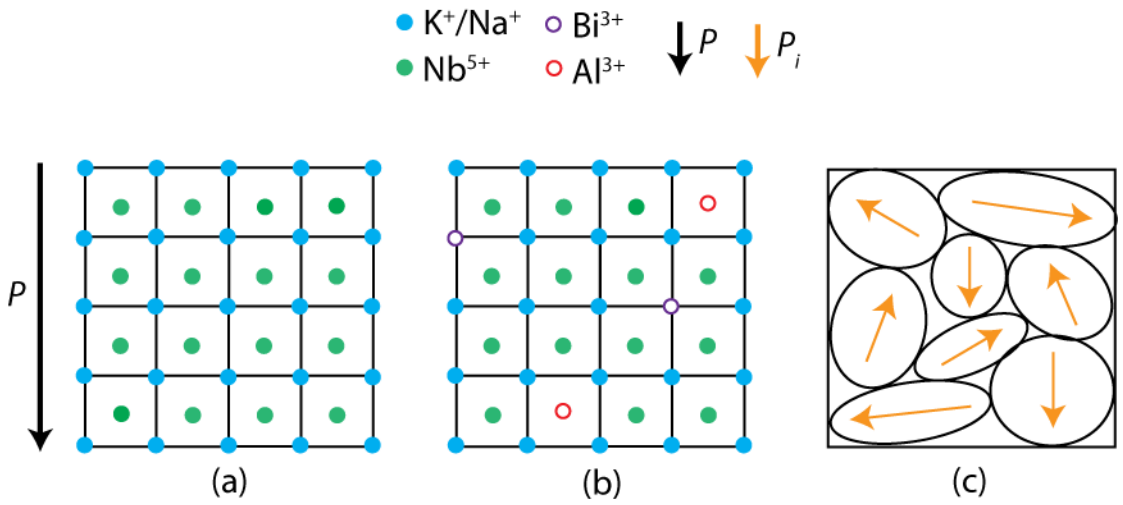

Figure 4.5: Schematics of crystal and polar structures: (a) homogeneous KNN lattice with single polarization direction (*P*) within a ferroelectric domain, (b) chemical disorder in the (1-*x*)KNN-*x*BA solid solution, and (c) breaking of ferroelectric long-range order into local polarizations (P_i) as a result of the chemical disorder shown in (b) (scale in (c) is larger than in (a) and (b) to represent multiple domains).

The coupled substitutions of Bi^{3+} for (K^+/Na^+) and Al^{3+} for Nb^{5+} introduce, however, the ions of different charges and different chemical nature on both the *A*- and *B*-sites. These ionic substitutions lead to chemical disorder and an inhomogeneous structure (Fig. 4.5(b)). The entire sample has the average solid solution composition, but local areas throughout the sample will have compositions that slightly deviate from the average as a result of chemical disorder. Since the Curie temperature is composition dependent, various areas will give rise to phase transitions at different temperatures, resulting in the diffuse peaks observed in the $\varepsilon'(T)$ variations. Internal stresses are also induced by the ionic substitutions of different radii (Table 4.1), which will affect the phase transition temperatures produced by those regions. Similar behaviour was observed in the $BaTiO_3$-$BaSnO_3$ solid solution [21].

Table 4.1: Charges and ionic radii of the *A*- and *B*-site ions in the KNN-BA solid solution system.

Site	Element	Ionic Charge	Ionic Radius (Å) [20]
A	K	1+	1.64
	Na	1+	1.39
	Bi	3+	1.17
B	Nb	5+	0.64
	Al	3+	0.535

Despite the small amount of BA introduced into KNN, the local chemical disorder is believed to affect the polar order of KNN significantly. It will weaken the ferroelectric coupling and break down the long-range polar (ferroelectric) order initially existing in the KNN material, giving rise to local polar regions of different orientation and different dipole moments (P_i), as shown in Fig. 4.5(c). These short-range polar regions will contribute to the permittivity differently than the non-substituted KNN. In particular, such an inhomogeneous polar structure contains a distribution of dielectric response times of various dipoles or local polarization (P_i), leading to the strong dispersion observed in the $\varepsilon'(f, T)$ variations in Figure 4.3.

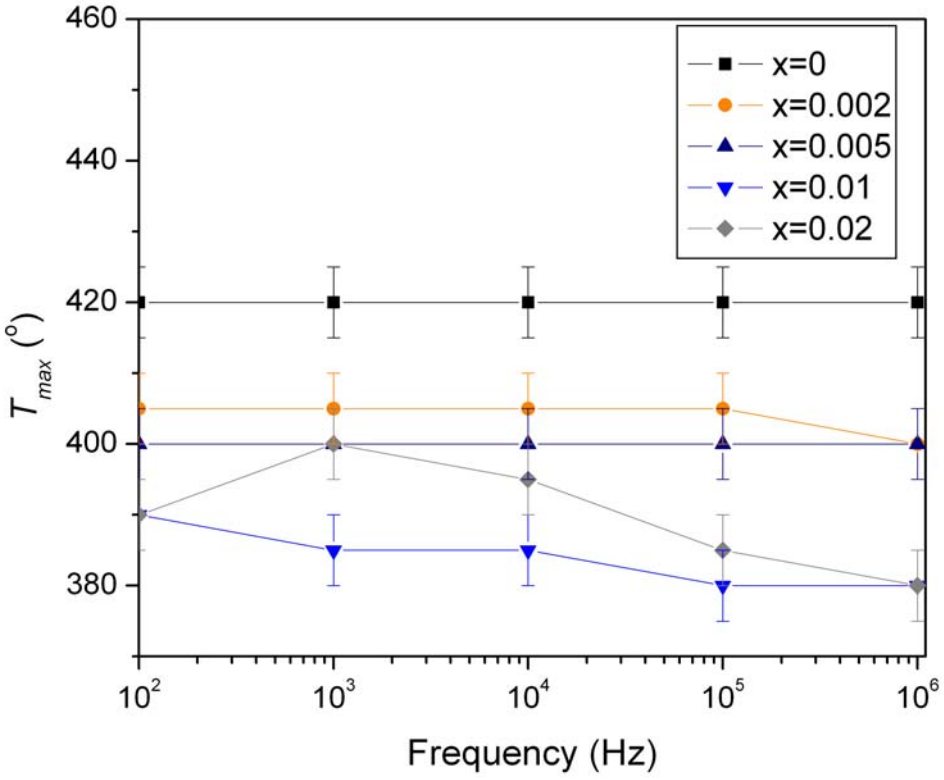

Figure 4.6: Frequency dependence of the maximum in the permittivity (T_{max}) of the (1-*x*)KNN-*x*BA solid solution ceramics (*x* = 0, 0.002, 0.005, 0.01 and 0.02).

Figure 4.6 shows the temperature of the maximum permittivity (T_{max}) as a function of frequency for the (1-*x*)KNN-*x*BA solid solution. The T_{max} remains constant through all frequencies (10^2 – 10^6 Hz) for $x \leq 0.005$, indicating no relaxation behaviour. However, for $x = 0.01$ and 0.02, the observed T_{max} increases with decreasing frequency, which is contrary to 'normal' relaxation, as found in relaxor ferroelectrics for example [19]. The change in behaviour is due to the overlapping contribution from low frequency dispersion (LFD) with the (diffuse) ferroelectric phase transition peak. The LFD mainly

results from mobile charge carriers within the sample, which leads to an increase in T_{max} and its magnitude ε'_{max} with decreasing frequency (the magnitude of ε'' and $tan\delta$ will also increase with decreasing frequency). Mobile charges are slowly moving carriers, but at high temperatures they are provided enough thermal activation energy to follow the AC current, allowing them to contribute more to the permittivity. For x = 0.01, there is a very small increase in T_{max} with decreasing frequency, however, there is a much greater increase in T_{max} observed for x = 0.02. This means that there are many more mobile charge carriers present, which is evidenced by the dramatic increase in dielectric loss for the x = 0.02 sample, as shown in Figure 4.3(f).

Figure 4.7 shows the variation of the maximum dielectric constant (ε'_{max}) as a function of composition (x = 0 - 0.02) at high (10^6 Hz) and low (10^2 Hz) frequencies. The high frequency data correspond to the ferroelectric behaviour (lattice contributions) of the materials, since mobile charge carriers cannot contribute to the permittivity at high frequency. The decreasing trend is a result of the increased diffuseness of the phase transition at T_C, which arises from the chemical and polar disorders from the addition of Bi^{3+} and Al^{3+}, as discussed previously. It can be seen that ε'_{max} values for the x = 0.01 and 0.02 samples are very similar, (and from Figure 4.3(d and e), both T_{max} values are 380 °C), which indicates that the ferroelectric contributions are very similar for these two samples at high frequencies. However, at low frequencies (10^6 Hz), the ε'_{max} in x = 0.02 increases compared with x =0.01, which indicates a stronger contribution from mobile charge carriers for x =0.02. This observation is consistent with the increased relaxation behaviour, as shown in Figure 4.6, where T_{max} increases with decreasing frequency more rapidly than in x =0.01.

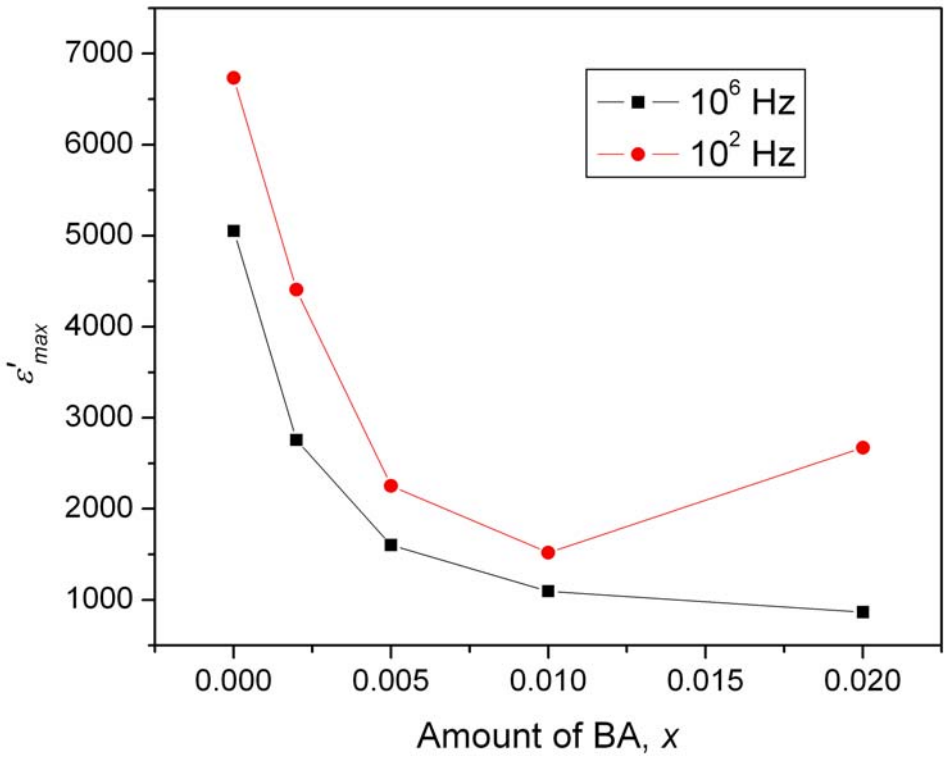

Figure 4.7: Composition dependence of the magnitude of the maximum in the permittivity (ε'_{max}) of the (1-*x*)KNN-*x*BA solid solution ceramics (*x* = 0, 0.002, 0.005, 0.01 and 0.02) at high and low frequency.

This low frequency dispersion is not the only effect being observed, however. For $x = 0.02$, it can be seen in Figure 4.6 that T_{max} shifts back to lower temperature at the lowest applied frequency of 10^2 Hz. This indicates that there are two or more overlapping processes. When a heterogeneous material, containing areas that exhibit different properties such as permittivity (ε) and conductivity (σ), is placed within an electric field, charges may be able to move across one area, but not the other (Fig. 4.8). This results in the build up of charge at the boundary and, thereby, the separation of charges known as Maxwell-Wagner polarization [22, 23].

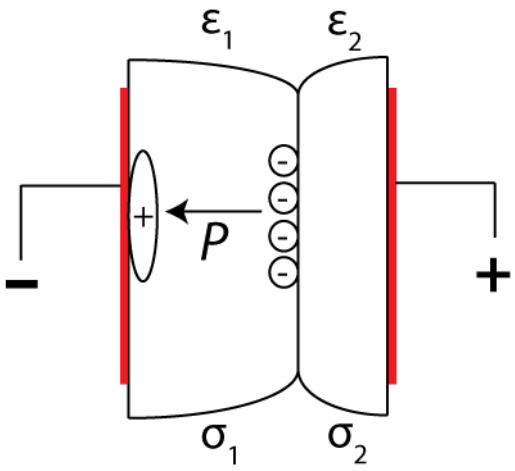

Figure 4.8: Illustration of Maxwell-Wagner polarization arising from the inhomogeneous polar microstructures.

These charges are separated over a large distance relative to the atomic scale, therefore, this polarization will have a much larger contribution to the dielectric response than the ferroelectric spontaneous polarizations developed in the material. The Maxwell-Wagner effect causes T_{max} to shift to lower temperatures with decreasing frequency [21, 22], so it seems likely that this is the dominant effect for the x = 0.02 sample at the frequency of 10^2 Hz.

4.4.3.3 Improved Dielectric Properties

Figure 4.9 shows the variation of the room temperature dielectric constant (ε'_{RT}) as a function of composition (x = 0 – 0.02) at a frequency of 10^6 Hz. It is apparent that ε'_{RT} increases significantly compared with pure KNN, reaching a maximum value of ε'_{RT} = 704 at x = 0.01, which is more than twice as large as the value of KNN ceramics. Therefore, the addition of a small amount of BA can effectively improve the dielectric

properties of the KNN ceramics. This can be attributed to the increased density and quality of the ceramics (see Fig. 4.2). Another factor affecting the room temperature dielectric constant is the local polarizations (P_i) created by the coupled substitutions of Bi^{3+} for $(K_{0.5}Na_{0.5})^{+}$ and Al^{3+} for Nb^{5+}, as discussed earlier in this section. The P_i are more polarizable, therefore, they will respond more easily to an electric field drive, leading to an enhanced ε'_{RT}. The inherent lone pair effect from the Bi^{3+} ion also contributes to an enhanced polarizability, and thereby, an increased room temperature dielectric constant in the solid solution ceramics.

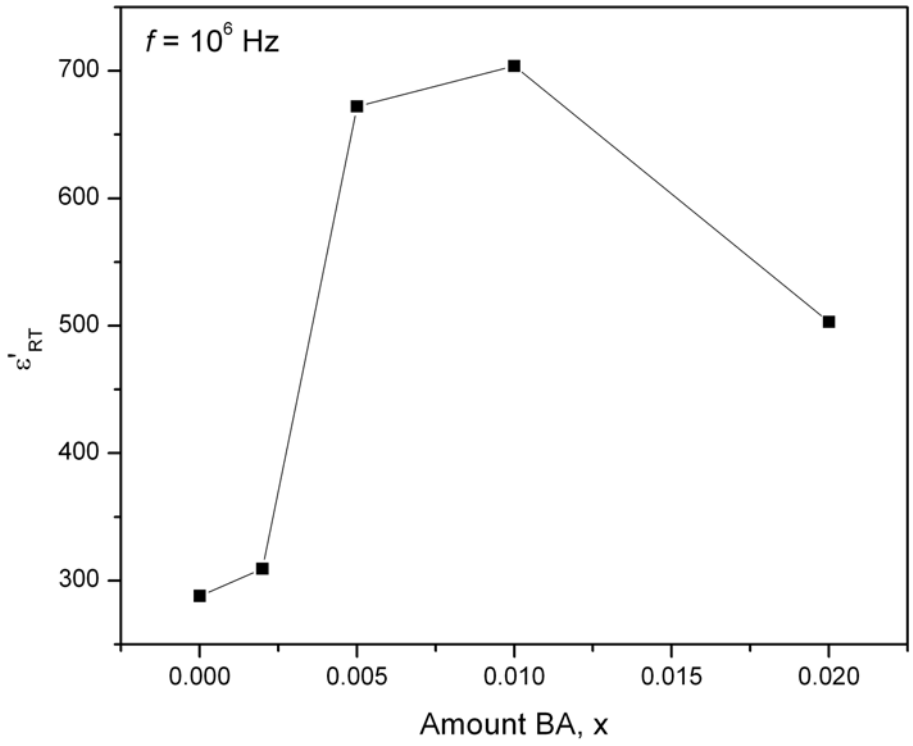

Figure 4.9: Composition dependence of the room temperature dielectric constant (ε'_{RT}) of the (1-*x*)KNN-*x*BA solid solution ceramics (*x* = 0, 0.002, 0.005, 0.01 and 0.02) measured at 10^6 Hz.

It should also be noted that the dielectric losses remain low (below 5 %) up to 400 °C for $x \leq 0.01$ for the (1-x)KNN-xBA solid solution (Fig. 4.3(f)), suggesting that the ceramics are of good dielectric quality, potentially useful for a large application temperature range. The improved dielectric properties of the KNN-BA ceramics, including increased ε'_{RT} and low loss, make them potentially useful for the fabrication of multilayered high-energy-density capacitors.

4.4.4 (Partial) Phase Diagram of the KNN-BA System

Based on the above structural analysis by XRD and phase transitions detected by the dielectric measurements as a function of temperature, a partial phase diagram between temperature and solid-solution composition is established in Figure 4.10, where T_C and T_I indicate the cubic (paraelectric) to orthorhombic (ferroelectric), and tetragonal (ferroelectric) to orthorhombic (ferroelectric) transition temperatures, respectively. This phase diagram delimits several phase zones on the KNN side of the solid solution, namely, cubic, tetragonal, orthorhombic and pseudo-cubic. In addition, a morphotropic phase boundary (MPB) is found to exist in the composition range of $0.002 \leq x \leq 0.005$ around room temperature, which bridges the orthorhombic phase and the pseudo-cubic phase. It can be seen that the cubic ↔ tetragonal phase transition temperature (T_C) decreases slightly with increasing x. In contrast, the tetragonal ↔ orthorhombic phase transition temperature (T_I) remains fairly constant (within error) up to x=0.01, above which it decreases.

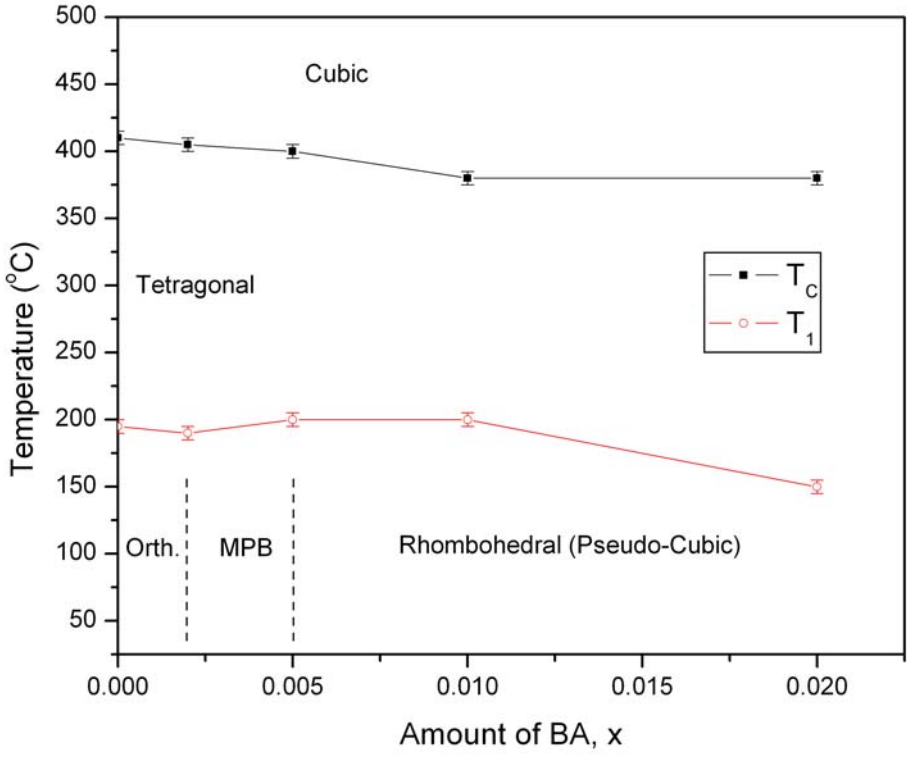

Figure 4.10: (Partial) temperature versus composition phase diagram of the (1-*x*)KNN-*x*BA solid-solution, where T_C and T_1 indicate the cubic (paraelectric) to orthorhombic (ferroelectric), and tetragonal (ferroelectric) to orthorhombic (ferroelectric) transition temperatures, respectively. This phase diagram delimits several phase zones on the KNN side of the solid solution, namely, cubic, tetragonal, orthorhombic and pseudo-cubic. In addition, a morphotropic phase boundary (MPB) is found to exist in the composition range of $0.002 \leq x \leq 0.005$ around room temperature.

4.4.5 Ferroelectric Characterization

Figure 4.11 shows the polarization versus electric field ($P(E)$) hysteresis loops at room temperature for the (1-x)KNN-xBA ceramics with x = 0, 0.005, 0.01, and 0.02, which indicate the ferroelectric properties of the solid solution. The x = 0.002 sample, however, exhibits conductive behaviour when measured.

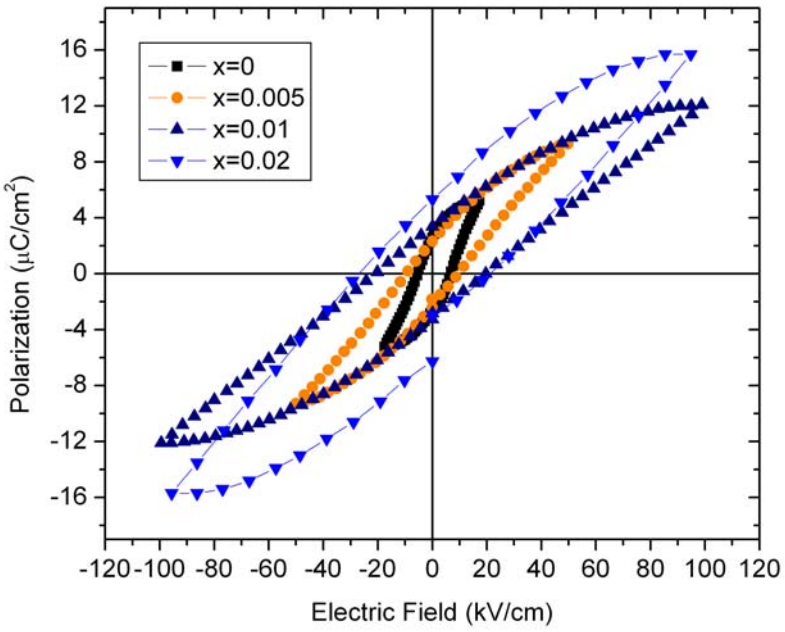

Fig. 4.11: Polarization-Electric Field (*P*-*E*) hysteresis loops of the (1-*x*)KNN-*x*BA solid solution ceramics (*x*=0, 0.005, 0.01 and 0.02), displayed at room temperature.

The KNN ceramic shows an apparent coercive field (E'_C) of 7 kV/cm and an apparent remnant polarization (P'_r) of 2.6 μC/cm^2, as the loop is not fully saturated with an applied field of 20 kV/cm. The ferroelectric loops for samples containing BA were not saturated with an applied field of up to 50 kV/cm for x = 0.005, and 100 kV/cm for x = 0.01 and 0.02. This arises from an increase of the coercive field (E_C) with the substitution

of BA which itself exhibits a high coercive field with non-saturated $P(E)$ hysteresis loops at room temperature [14]. Attempts were made to measure the $P(E)$ loops and the ferroelectric properties at high temperatures with a view to saturating the loops (because E_C is expected to decrease as temperature increases), but the samples either became conducting or broke down.

Table 4.2: Apparent remnant polarization (P'_r) arising from applied electric field (E_{max}) for the (1-x)KNN-xBA ceramics of various BA content (x).

x	P'_r (mC/cm^2)	E_{max} (kV/cm)
0	2.58	17
0.005	2.33	50
0.01	3.39	100
0.02	5.33	100

As a result of high coercivity, only the apparent remnant polarization (P'_r) and the apparent coercive field (E'_C), displayed on the $P(E)$ loops, are studied as a function of composition. The P'_r is tabulated as a function of BA content (x) and shown in Table 4.2. An increase in polarization is found with x = 0.01 and 0.02, reaching a maximum of 5.3 μC/cm^2 for the x = 0.02 sample. The P'_r for x = 0.005 is included in Table 4.2, but it should be noted that it cannot be easily compared to the x = 0.01 and 0.02 samples because the maximum field applied was only 50 kV/cm, instead of 100 kV/cm. The increase of the remnant polarization of the KNN-BA solid solution over that of pure KNN can be attributed to the introduction of the Bi^{3+} ions, which have a lone pair of 6*s* electrons. This stereochemically active lone pair of Bi^{3+} seems to enhance the spontaneous polarization of the material greatly. It is reasonable to anticipate that, if a

large enough field could be applied, a much higher P_r would be achieved, as was observed for the NBT-BA ceramics (P_r = 52 μC/cm^2) [16].

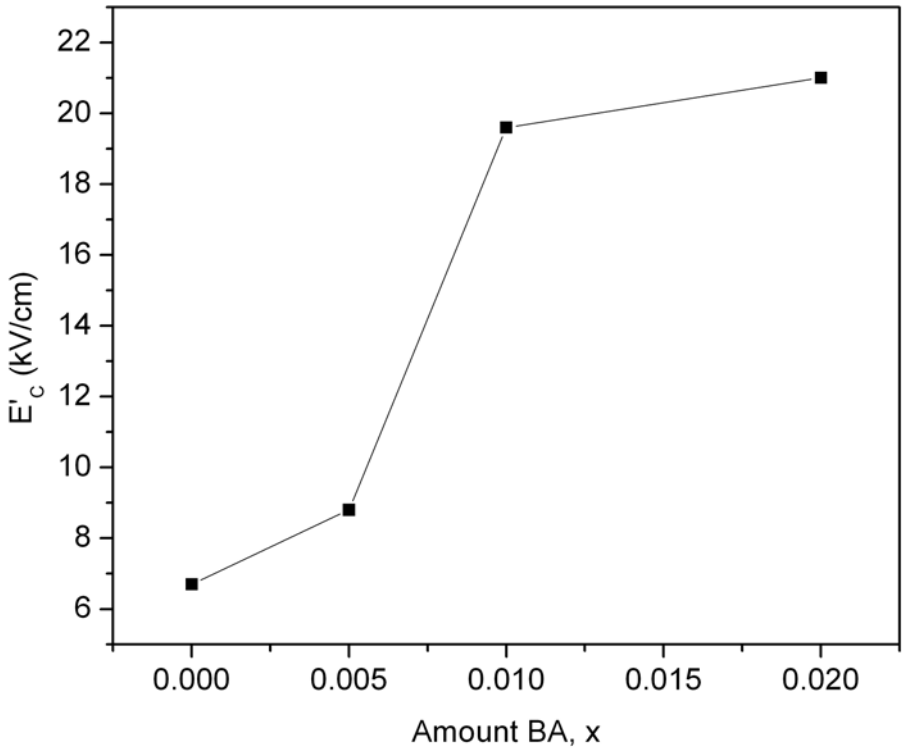

Figure 4.12: Apparent coercive field (E'_C) as a function of BA content (x).

The apparent coercive field (E'_C) is plotted as a function of BA content (x), as shown in Fig. 4.12. It is obvious that the coercive field is increased significantly with the addition of BA over that of pure KNN. As the coercive field of pure BA was found to be quite high (> 50 kV/cm at room temperature) [14], it is natural that introducing BA should increase the coercive field of pure KNN since it has a much lower E_C than BA to begin with. This observation is consistent with the chemical feature of the Bi^{3+} ion lone

electron pair, which enhances the polar bonds, stabilizes the polarization and prevents it from being easily switched (reoriented).

Although a higher E_C means a more stable polar state, it also makes it more difficult to pole the samples. In an attempt to overcome this problem, the x = 0.005 sample was heated above the T_1 phase transition, and a field of 30 kV/cm was applied for 10 minutes, after which the sample was cooled down to room temperature with the field kept on. This high temperature poling did not seem to be effective, as the measured piezoelectric coefficient remains the same as the room temperature poled sample (d_{33} = 20 pC/N), meaning that no further alignment of polarization was achieved.

The large E_C also prevents the potentially enhanced piezoelectric properties from being realized even though the existence of an MPB suggests that high piezoelectric properties could be expected. Further work in chemical modifications (e.g. by doping with "softening" ions of La^{3+}, $Sb^{3+/5+}$, Ta^{5+}, or W^{6+} [24-26]) of this solid solution system is necessary in order to decrease the coercive field (here "softening" means reducing the energy barrier between the potential wells so that polarization can be switched from one state to the other). On the other hand, the large E_C may be useful in specific applications since materials with large coercive fields are utilized in high-power piezoelectric transducers as it allows for a larger field to be applied without switching polarization.

4.5 Conclusions

A pure perovskite phase was synthesized in the (1-x)KNN-xBA solid solution for x < 0.05. Dense ceramics were produced, reaching a maximum relative density of 96.7%. Such a significantly improved densification entitles the KNN-BA ceramics as promising

lead-free materials for piezoelectric and ferroelectric applications. The coupled substitutions of Bi^{3+} for K^{+} and Na^{+} on the *A* site and Al^{3+} for Nb^{5+} on the *B* site lead to the transformation of the orthorhombic symmetry of KNN into a rhombohedral (pseudo-cubic) phase at room temperature. A morphotropic phase boundary (MPB) is found to be present in the composition range of $0.002 \leq x \leq 0.005$, which bridges the orthorhombic and rhombohedral phases. With increasing *x*, the peaks in $\varepsilon'(T)$ become more broadened as a result of increased diffuseness of the transition. Significant frequency dispersion is also found in the ceramics with $x > 0.002$, which has been discussed based on the chemical and polar disorder structural models, as well as the contribution from mobile charges. Significant increase in the room temperature permittivity (ε'_{RT}) was achieved due to improved density and quality of the ceramics, as well as enhanced polarizability in the materials as a result of the cationic substitutions. The increased ε'_{RT} makes the KNN-BA ceramics useful for high-energy density capacitor applications to replace currently used PZT- and PMN-based materials.

With respect to ferroelectric properties, the remnant polarization is found to increase with increasing *x* and the coercive field is also increased over that of KNN, which makes it difficult to fully saturate the ferroelectric hysteresis loops as quite often the $E_C > E_{breakdown}$. This increase in E_C makes the ceramics more difficult to pole, and therefore, the piezoelectric coefficient measured for the $x = 0.005$ sample is relatively low ($d_{33} = 20$ pC/N). On the other hand, the enhanced E_C makes the materials useful for high-power electromechanical transducer applications.

References:

[1] G.H. Haertling, J. Am. Ceram. Soc. **82**, 797 (1999).

[2] B. Jaffe, W.R. Cook, and H. Jaffe, Piezoelectric Ceramics (Academic, London, 1971), p. 135-183.

[3] R.E. Jaeger and L. Egerton, J. Am. Ceram. Soc. **45**, 209 (1962).

[4] G.H. Haertling, J. Am. Ceram. Soc. **50**, 329 (1967).

[5] H. Birol, D. Damjanovic, and N. Setter, J. Eur. Ceram. Soc. **26**, 861 (2006).

[6] M. Kosec and D. Kolar, J. Am. Ceram. Soc. **10**, 335 (1975).

[7] Y. Guo, K. Kakimoto, and H. Ohsato, Appl. Phys. Lett. **85**, 4121 (2004).

[8] Y. Guo, K. Kakimoto, and H. Ohsato, Mater. Lett. **59**, 241 (2005).

[9] G.-Z. Zang, J.-Feng Wang, H.-C. Chen, W.-B. Su, C.-M. Wang, P. Qi, B.-Q. Ming, J. Du, L.-M. Zheng, S. Zhang, and T.R. Shrout, Appl. Phys. Lett. **88**, 212908 (2006).

[10] R. Wang, R.-J. Xie, K. Hanada, K. Matsusaki, H. Bando, and M. Itoh, Phys. Status Solidi A **202**, R57 (2005).

[11] Y. Guo, K. Kakimoto, and H. Ohsato, Jpn. J. Appl. Phys., Part 1 **43**, 6662 (2004).

[12] C. Lei and Z.-G. Ye, Appl. Phys. Lett. **93**, 042901 (2008).

[13] A. A. Belik *et al*., Chem. Mater. **18**, 133 (2006).

[14] J. Zylberberg, A.A. Belik, E. Takayama-Muromachi, and Z.-G. Ye, Chem. Mater. **19**, 6385 (2007).

[15] H. Yu and Z.-G. Ye, J. Appl. Phys. **103**, 034114 (2008).

[16] H. Yu and Z.-G. Ye, Appl. Phys. Lett. **93**, 112902 (2008).

[17] M. Kosec and D. Kolar, J. Am. Ceram. Soc. **10**, 335 (1975).

[18] E. I. Speranskaya, V. M. Skorikov, G. M. Safronov, and E. N. Gaidukov, Inorg. Mater. (Engl. Transl.) **6**, 1201 (1970).

[19] A. A. Bokov and Z.-G. Ye, J. Mater. Sci. **41**, 31 (2006).

[20] R. D. Shannon, Acta Cryst. **A32**, 751 (1976).

[21] G. A. Smolensky, J. Phys. Soc. Jap. **28**, (1970).

[22] R. Wagner, Arch. Elektrotech. **2**, 371 (1914).

[23] R. Sillars, J. Inst. Elect. Eng. **80**, 378 (1937).

[24] J. F. Tressler, S. Alkoy, and R. E. Newnham, J. Electroceram. **2**, 257 (1998).

[25] G. H. Haertling, Ceramic Materials for Electronics, Processing, Properties, and Applications, ed. by R. C. Buchanan (Marcel Dekkar, New York, 1986), p. 165.

[26] Y. Xu, Ferroelectric Materials and Their Applications (North-Holland, Amsterdam, 1991), p. 217, 277.

CHAPTER 5:
General Conclusions and Future Directions

5.1 General Conclusions

As discussed in Chapter 1, the majority of the high-performance piezoelectric and ferroelectric materials currently used contain lead. However, biological and environmental concerns require the scientific community to develop alternative lead-free materials with high performance and large temperature operating ranges for electromechanical transducer applications. The work presented in this thesis is centred around the challenging task of developing new lead-free materials for the replacement of lead-containing piezo-/ferroelectric ceramics. New chemical processes have been used in the synthesis of these materials, and various analytical and measurement techniques have been employed to characterize the structures and the dielectric, piezoelectric and ferroelectric properties of the materials synthesized, in order to deduce the reaction mechanism and to understand the synthesis - (micro)structure - property relations.

Improving the sinterability of KNN and thereby preparing its ceramics of enhanced properties by a new synthetic process, have been the focus of the first part of this thesis work. Potassium fluoride (KF) has been successfully used as a sintering agent to produce dense ceramics of KNN, with an increased relative density reaching 92%. Piezoelectric properties were improved over those of conventionally sintered KNN ceramics. The SEM imaging revealed that the ceramics sintered with KF were less porous than the KNN ceramics. This enhanced densification correlates well with the improved electrical properties. The Curie temperature is unaffected by the addition of KF and remains high and unchanged at 420 °C, which indicates that KF was not incorporated

into the perovskite structure of KNN. Structural and chemical analyses were performed by means of XRD, EDS, and XPS to deduce the sintering mechanism, and the results confirm that the fluoride does not enter the lattice of KNN. In fact, KF forms a transient liquid phase at the grain boundaries of KNN, which promotes grain growth and, thereby, the densification of the ceramics. It then evaporates in the final stages of the sintering process. The KF-aided sintering is shown to be a simple, inexpensive and effective technique, which can be used to produce dense KNN-based ceramics with improved dielectric and piezoelectric properties potentially useful in electromechanical transducer applications over a wide temperature operation range.

The $(1\text{-}x)K_{0.5}Na_{0.5}NbO_3\text{-}xBiAlO_3$ (KNN-BA) solid solution has successfully been prepared, demonstrating that BA can be partially stabilized in the crystal lattice of KNN. The relative densities of the solid solution ceramics were found to increase with increasing x, reaching as high as 96.7%. A partial temperature-composition (T-x) phase diagram has been established based on dielectric and XRD studies, which includes a morphotropic phase boundary (MPB) in the composition range of $0.002 \leq x \leq 0.005$. With increasing x, the peaks in $\varepsilon'(T)$ become more broad indicating that the structural phase transitions in KNN become more and more diffuse, while significant frequency dispersion is also exhibited by ceramics with $x > 0$. This dispersion arises from the introduction of Bi^{3+} and Al^{3+} ions on the A and B sites, respectively, which leads to structural and polar disorders in the material. Significant increase in the room temperature permittivity (ε'_{RT}) was observed due to increased density and quality of the ceramics, as well as enhanced polarization in the materials as a result of the cationic

substitutions. The increased ε'_{RT} makes the KNN-BA ceramics useful for high-energy density-capacitor applications to replace currently used PZT- and PMN-based materials.

The remnant polarization is also found to increase with the addition of BA, so it is clear that the stereochemically active lone pair of electrons of Bi^{3+} enhance the polarization of the material as expected. The coercive field is also increased over that of KNN, which makes it more difficult to pole the ceramics completely, resulting in relatively low measured piezoelectric properties. On the other hand, the increased coercive fields make the KNN-BA ceramics useful in high-power electromechanical transducer applications.

5.2 Future Directions

The sintering problem of KNN ceramics is very important in the development of lead-free materials as high quality materials are essential for various applications. KNN is one of the most promising environmentally friendly piezoelectric systems, so the ability to overcome its sintering issues has opened up new opportunities for this family of materials in devices applications. Compared with the currently used sintering methods, such as hot-pressing and texturing, which are complicated and expensive, the KF-aided sintering is shown to be a simple and cost-effective technique, which leads to improved properties. It would be interesting to employ this technique in the synthesis of other lead-free systems and to study its effect. It is expected, upon optimization of the process, that the KF-aided sintering could enhance the properties of appropriate lead-free materials systems such that they are closely compared to the properties of current lead-containing materials. It may also be interesting to develop thin films of these materials for

applications in microelectromechanical systems (MEMS) and other electromechancial transducer applications.

The synthesis of the KNN-BA solid solution has contributed to the investigation and improvement of lead-free materials. The formation of the solid solution has addressed both the sintering problem of KNN, as the density of ceramics has been increased, and the need for high pressure sintering of BA, as it can be partially stabilized within the KNN crystal lattice. However, the large coercive fields exhibited by these solid solution ceramics make the potentially enhanced piezoelectric properties hard to be realized. Further investigation of this system in terms of chemical modifications, for example with softening ions like La^{3+}, $Sb^{3+/5+}$, Ta^{5+}, or W^{6+}, appears to be rewarding. The introduction of donor-type cations have proven to decrease the coercive field in PZT and related materials (e.g. with the introduction of La^{3+}). The same approach is expected to be effective in lowering the coercive field of the KNN-BA ceramics. This would enable the ceramics to be fully poled, and their potentially enhanced piezoelectric properties to be realized. From a crystal chemistry point of view, the KNN-BA system is similar to lead-containing systems, such as PZT, due to the observed MPB and the presence of the stereochemically active lone pair of Bi^{3+}, so it may show very good piezo-/ ferroelectric properties if investigated further. From a crystal physics point of view, the origin of diffuse phase transitions, dielectric dispersion and relaxation, which is associated with the chemical and polar order/disorder induced by the coupled substitution of $Bi^{3+} + Al^{3+} \rightarrow (K_{0.5}Na_{0.5})^{+} + Nb^{5+}$, needs to be studied more in-depth by broad-band dielectric spectroscopy and electronic characterization as well as appropriate modeling, in order to

better understand the structure – property relation in this interesting solid-solution system.